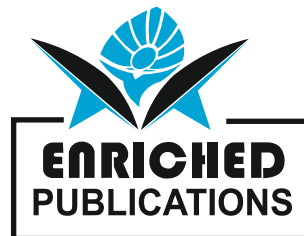


Journal of Aerospace Science and Applications

Volume No. 10
Issue No. 1
January - April 2025



ENRICHED PUBLICATIONS PVT.LTD

**JE - 18,Gupta Colony, Khirki Extn,
Malviya Nagar, New Delhi - 110017.**

E- Mail: info@enrichedpublication.com

Phone :- +91-8877340707

Journal of Aerospace Science and Applications

Aims and Scope

The Journal of Aerospace Science and Applications published three issues yearly by Enriched publications. Journal of Aerospace Science and Applications is peer reviewed journal and monitored by a team of reputed editorial board members. This journal consists of research articles, reviews, and case studies on Aerospace Research. This journal mainly focuses on the latest and most common subjects of its domain.

Authors are invited to submit papers on new advances in the following topics to aerospace applications:

- Materials and structures
- Flight mechanics
- Navigation, guidance and control
- Electromagnetism and radar
- Signal and image processing
- Information processing
- Human behaviour
- Robotics and intelligent systems

Journal of Aerospace Science and Applications

**Managing Editor
Mr. Amit Prasad**

Journal of Aerospace Science and Applications

(Volume No. 10, Issue No. 1, Jan - Apr 2025)

Contents

Sr. No	Articles/Authors	Pg No
01	Analysis of the Landsat-1 Rocket Fragmentation in Orbit Using Theory and Computations <i>- Arjun Tan*, Almuatasim Alomari and Marius Schamschula</i>	1 - 10
02	Velocity Perturbations Analysis of the Fragmentation of USA-193 Satellite in Orbit <i>- Arjun Tan¹ and Robert C. Reynolds²</i>	11 - 20
03	Posthumous Analysis of the Indian Anti-Satellite Experiment Part III: A Plausible Fragmentation Scenario <i>- Arjun Tan</i>	21 - 30
04	Investigating the YunHai 1-02 Satellite Fragmentation using Theory and Velocity Perturbations Analysis of its Fragments <i>- Arjun Tan</i>	31 - 40
05	Investigating Russia's Direct-Ascent Anti-Satellite Test <i>- Arjun Tan</i>	41 - 53

Analysis of the Landsat-1 Rocket Fragmentation in Orbit Using Theory and Computations

Arjun Tan*, Almuatasim Alomari and Marius Schamschula
Department of Physics, Alabama A & M University, Normal, AL 35762, U. S. A.

ABSTRACT

The Landsat-1 second stage Delta rocket was the second among several such rocket bodies to have exploded following the successful mission in placing its payload in orbit. The assessed cause of each of these explosions was the ignition of residual propellants left in the rocket bodies. In this study, we examine the Landsat-1 rocket body explosion using theory and computations. The Gabbard diagram of the fragments departed significantly from the inclined 'X' shape for those of circular orbits due to the small eccentricity of the parent satellite and orbital drag. The shape of the Gabbard diagram with a 'cavity' in the middle indicated that the fragmentation took place midways between the apogee and perigee. The scatterplots of the velocity perturbation components in three mutually perpendicular planes indicated that the rocket body likely exploded in the Octant model of exploding tanks. The largest remnant of exploded rocket suffered unusually large velocity perturbations in all three directions. A noticeably large concentration of fragments on the opposite side of the parent RB suggests that there was a possible recoil effect between these fragments and the largest remnant. The angular distribution of the fragments in a cylindrical projection map substantiates this finding.

INTRODUCTION

Within a span of eight years between 1973 and 1981, no fewer than seven Delta second stage rocket bodies (RB) had exploded in low-Earth orbit at various intervals following the successful performance of their missions. The explosion of Landsat-1 second stage RB (International Designator 1972-58B; U.S. Satellite Number 6127) was the second of these events which took place at 1827 GMT on 22 May 1975 over southern Indian Ocean. The assessed cause of each of these explosions was the ignition of residual propellants left in the rocket bodies. Corrective actions were implemented in the aftermath of venting out the residual propellants upon completion of the mission. Initial studies of these explosions had been reported [1 – 3]. In this paper, we re-examine the Landsat-1 RB explosion by (1) examining the Gabbard diagram of the orbits of the fragments produced; and (2) calculating and analyzing the magnitudes and directions of the fragment velocities. The method of Badhwar, et al. [4] is used for the latter purpose. The event location and relevant data are taken from History of on-orbit Satellite Fragmentations [5]. The data for the orbital elements of the fragments are taken from Space-track.org [6].

GABBARD DIAGRAM OF THE FRAGMENTS

The Gabbard diagram is one of the earliest tools to investigate a satellite fragmentation in orbit. It is a plot of the apogee and perigee heights, h_A and h_P , respectively, of the fragments as functions of their periods, P . For a satellite having semi-major axis a and eccentricity e , the apsidal heights are given by

$$h_A = a(1 + e) - r_{\oplus} \quad (1)$$

and
$$h_P = a(1 - e) - r_{\oplus} \quad (2)$$

where r_{\oplus} is the reference radius of the Earth, and

$$a = \sqrt[3]{\frac{GM}{n^2}} \quad (3)$$

Is the semi-major axis, GM the gravitational parameter of the Earth and n the *mean motion* of the satellite. The period, by definition is, $P = 2\pi/n$.

The Gabbard diagram has distinguishing patterns depending upon the eccentricity of the fragmenting satellite's orbit and its true anomaly at the point of fragmentation which therefore can shed light regarding the fragmentation. Various classes of Gabbard diagrams are found in the literature [7].

VELOCITY PERTURBATIONS OF THE FRAGMENTS

The second and more important tool to analyze a satellite fragmentation event consists of calculating the velocity perturbations of the fragments from their orbital elements. Exact solutions of the three orthogonal components of the velocity perturbation of a fragment in the radial, down-range and cross-range directions of the parent satellite denoted by dv_r , dv_d and dv_x , respectively, were obtained [4] as follows:

$$dv_r = \pm \sqrt{\mu \left(\frac{2}{r} - \frac{1}{a'} \right) - \frac{\mu a'}{r^2} (1 - e'^2)} - v_r \quad (4)$$

$$dv_d = \frac{\cos \zeta}{r} \sqrt{\mu a' (1 - e'^2)} - v_d \quad (5)$$

Analysis of the Landsat-1 Rocket Fragmentation in Orbit Using Theory and Computations

and
$$dv_x = \frac{\sin \zeta}{r} \sqrt{\mu a' (1 - e'^2)} \quad (6)$$

where v_r and v_d are respectively the radial and down-range components of the velocity of the parent satellite at the point of fragmentation; a' and e' are respectively the semi-major axis and eccentricity of the fragment's orbit; and r is the radial distance of the fragmentation point from the centre of the Earth. The plane-change angle of the fragment's orbit is

$$\zeta = \pm \cos^{-1} \frac{\cos i \cos i' + \sqrt{(\cos^2 \lambda - \cos^2 i)(\cos^2 \lambda - \cos^2 i')}}{\cos^2 \lambda} \quad (7)$$

where i and i' are the respective inclinations of the parent and fragment's orbits, respectively and λ is the latitude of the fragmentation point. In Eq. (4), the + and – signs correspond to the ascending and descending modes of the fragment, respectively; and in Eq. (7), the + sign corresponds to $i' > i$ and the – sign corresponds to $i' < i$ on the northbound orbits with the opposite sense on the southbound orbits [4].

RESULTS

The fragmentation of Landsat-1 RB took place on 22 May (Day 143) 1975 at 18:27 GMT above southwest Indian Ocean at 34oS latitude and 46oE longitude [5]. This was the second Delta upper stage to experience breakup in orbit, after the NOAA-3 upper stage in 1973. The event occurred 34 months after successful deployment of the Landsat-1 payload [5]. The pre-event orbital elements data of the fragmenting RB were of Day 142 of 1973 [6]. In accordance with the latter, the satellite had inclination of $i = 98.3439^\circ$; eccentricity $e = .0193108$; and mean motion $n = 14.36209995$ rev/day. The data for the satellite yield: $P = 100.2638893$ min; $a = 7,149.188234$ km; $h_a = 909.09978$ km; $h_p = 632.98669$ km; $v_d = 7,508.624696$ km/s; and $v_r = -138.447505$ m/s. The data for the orbital elements of the fragments are taken from Space-track.org [6]. Altogether 114 fragments including the largest remnant and catalogued through Day 229 of 1975 were taken into consideration. Fragments catalogued subsequently (after February 1976) were ignored because Landsat-2 RB had fragmented by then in the same vicinity of altitude and inclination and there was the possibility of cross-cataloguing between the Landsat-1 and Landsat-2 Rbs.

Fig. 1 is the Gabbard diagram of the 114 fragments of Landsat-1 RB, including the largest remnant. Since the orbit of the rocket body prior to fragmentation was slightly eccentric (as indicated by e , h_a and h_p), the Gabbard diagram departed from the classical 'X' form for circular orbits. Firstly, the perigee line on the right side of the inclined 'X' had a small slope from the horizontal. Secondly, left side of the 'X' had degenerated into the 'claw' shape due to drag effects. Even though the fragmentation took place at 730 km altitude, the retrograde v_d 's suffered by the fragments on the left side had evidently lowered the perigee heights substantially to have caused this effect. Finally, there is a discernible 'cavity' devoid of fragments around the intersection point of the two arms of the 'X' which occurs when the fragmentation altitude (730 km in this case) is about midway between h_a and h_p (909 km and 633 km, respectively, in this case). This happens for low eccentricity fragmenting satellites, since there is greater probability of enhancement, than of diminution, of eccentricities of the fragments produced.

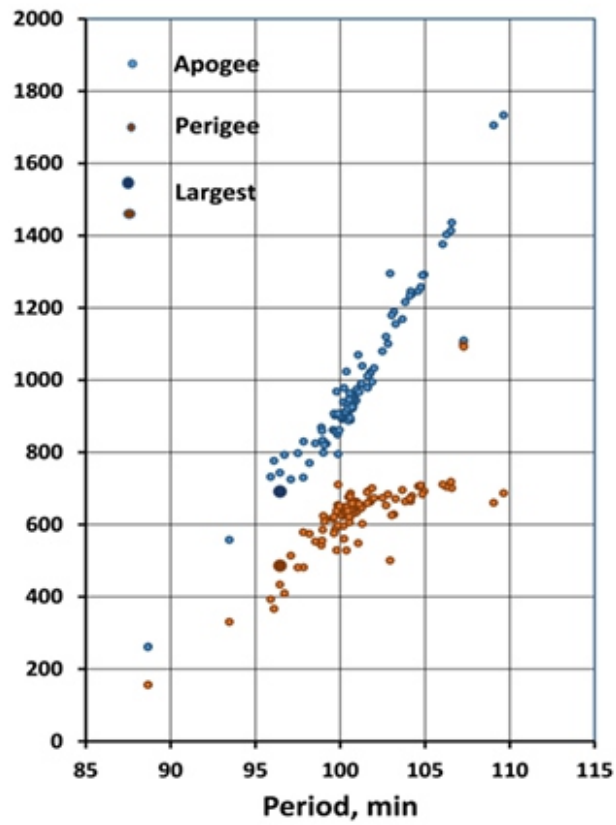
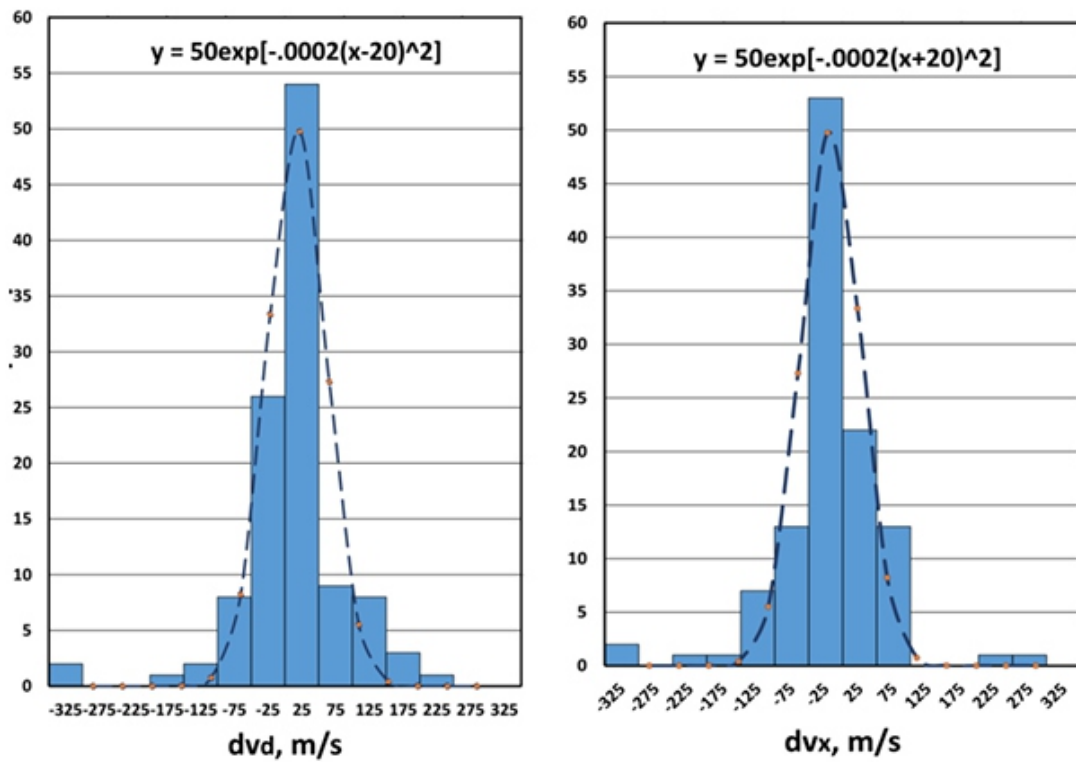


Fig. 1. Gabbard diagram of fragments of Landsat-1 RB.



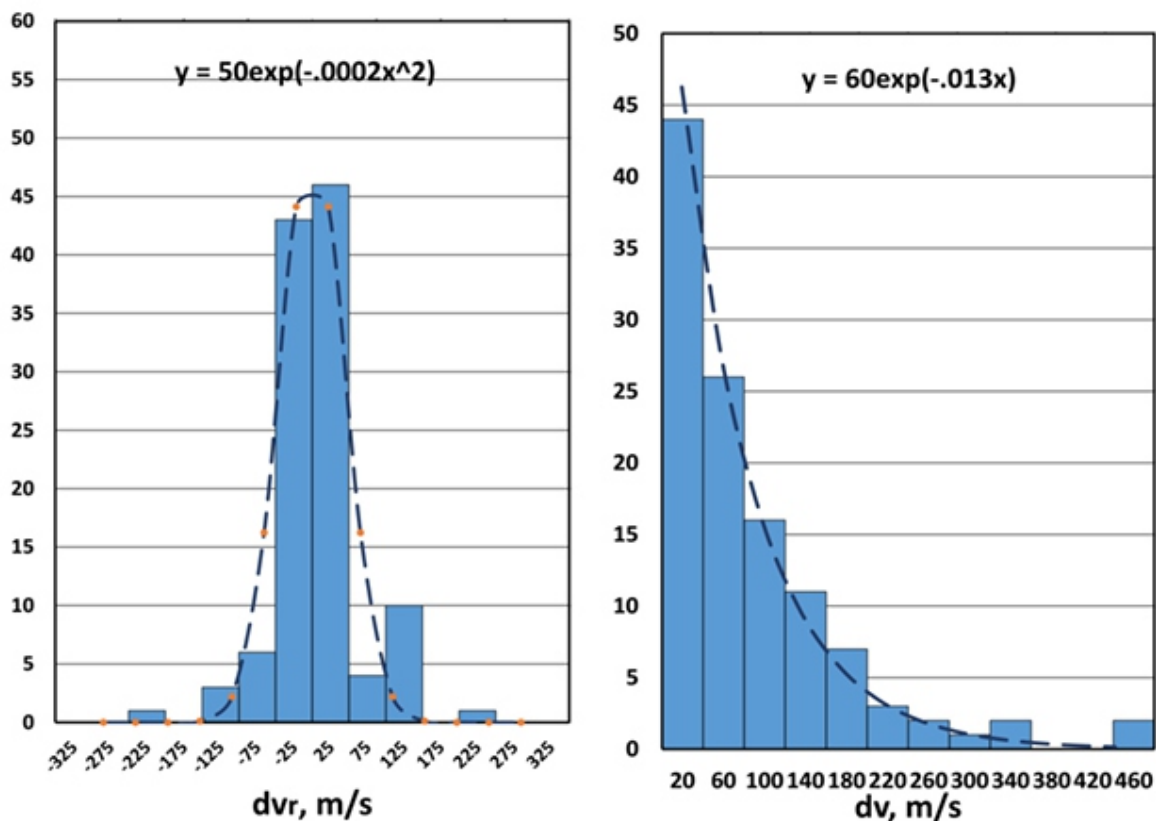


Fig. 2. Frequency distributions of the velocity perturbations of the fragments of Landsat-1 RB.

The velocity perturbations of the Landsat-1 RB fragments, including those of the largest remnant, were calculated using Eqs. (4)–(7). The frequency distributions of dvd , dv_x , dvr and dv of the fragments are shown in Fig. 2, together with their fitted curves. The distributions of dvd , dv_x and dvr are by and large Gaussian. The distribution of dvd is shifted in the forward direction, which could imply that fragments with retrograde down-range velocity perturbations had selectively deorbited. The dv_x distribution, on the other hand, is shifted in the negative direction, which means that looking vertically down the horizontal plane, more fragments headed to the right of the parent satellite’s motion. Both of these displacements were in the opposite direction of the largest remnant ($dvd = -95.789$ m/s; $dv_x = 28.405$ m/s). The inference drawn would be that the largest remnant had to have a considerable mass to oppose a large number of fragments. The distribution of dv is nearly exponential, similar to that of the NOAA-3 RB fragments [8] and in contrast to the beta distribution found in an earlier study [4].

The scatterplots of velocity perturbation components of the Landsat-1 RB fragments (including the largest remnant) are shown in three mutually perpendicular planes in Fig. 3: (1)

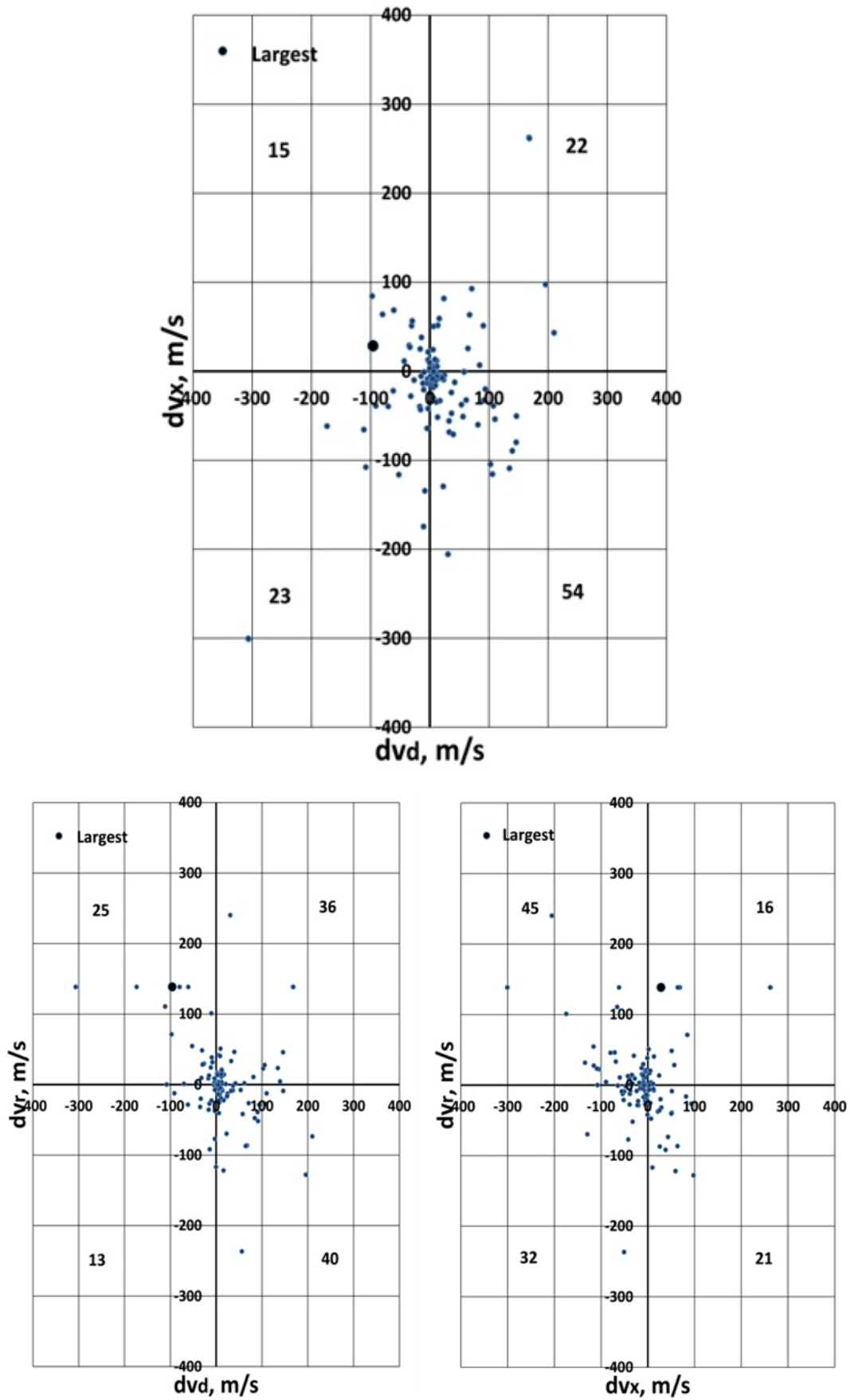


Fig. 3. Scatterplots of the velocity perturbation components of Landsat-1 RB fragments.

In the horizontal plane, viewed from vertically below; (2) In a vertical plane containing the momentum of the parent; and (3) In another vertical plane containing the angular momentum of the parent. The numbers of fragments in each quadrant of the three planes are also marked. Conspicuously, the largest remnant (which inherits the satellite number of the parent RB) suffered significant displacements from its fragmenting location (the origin). Significantly too, it is generally found in the quadrant opposite to that containing the largest (first two plots) or the second largest (third plot) number of fragments. This explains the large velocity perturbations suffered by the largest remnant. Overall the pattern of the fragments is roughly isotropic with an abundance of fragments with small velocity deviations surrounding the origin. The first part of the statement meant that the Landsat-1 RB most likely fragmented in the Octant Model of fragmenting tanks in the PISCES Model [9]; and the last part of the statement explains the exponential distribution of the total velocity perturbations dv of the fragments in Fig. 2. This is consistent with the explosive fragmentation of the NOAA-3 RB [8] as opposed to an earlier study [4].

Table I. Orbital Elements Change and Velocity Perturbations of Fragments					
Fragments with $a' > a^1$	Fragments with $a' < a^1$	Fragments with $i' > i^2$	Fragments with $i' < i^2$	Fragments with $e' > e^3$	Fragments with $e' < e^3$
77	37	37	77	71	43
Fragments with $dv_d > 0$	Fragments with $dv_d < 0$	Fragments with $dv_x > 0$	Fragments with $dv_x < 0$	Fragments with $dv_r > 0$	Fragments with $dv_r < 0$
76	38	37	77	61	53
$^1a = 7149.188 \text{ km}$		$^2i = 98.3439^\circ$		$^3e = .019308$	

Table I shows the numbers of fragments which gained or lost energy ($a' > a$ or $a' < a$), suffered inclination changes ($i' > i$ or $i' < i$), or eccentricity changes ($e' > e$ or $e' < e$). Also shown in the Table I are the numbers of fragments suffering positive and negative velocity perturbations in the down-range, cross-range and radial directions. The very significant correlations between the two sets of numbers can be explained as follows. For a nearly circular orbit ($e \approx 0$), it was shown that [8]:

$$da \approx \frac{2}{n} dv_d \quad (8)$$

$$di \approx \frac{\cos u}{na} dv_x \quad (9)$$

and

$$de \approx \frac{\sin \theta}{na} dv_r \quad (10)$$

Stated in words, dv_d , dv_x and dv_r were highly correlated with da , di and de , respectively. The less than perfect correlation in this case, especially between dv_r and de , is because the parent RB had a slight eccentricity, and also due to the possibility that several fragments with positive dv_r may well have de-orbited.

Fig. 4 gives a three-dimensional perspective of the dv_d , dv_x and dv_r of the fragments in the local right-handed system of coordinates. The locations of the parent satellite at fragmentation and its largest remnant are marked in the figure.

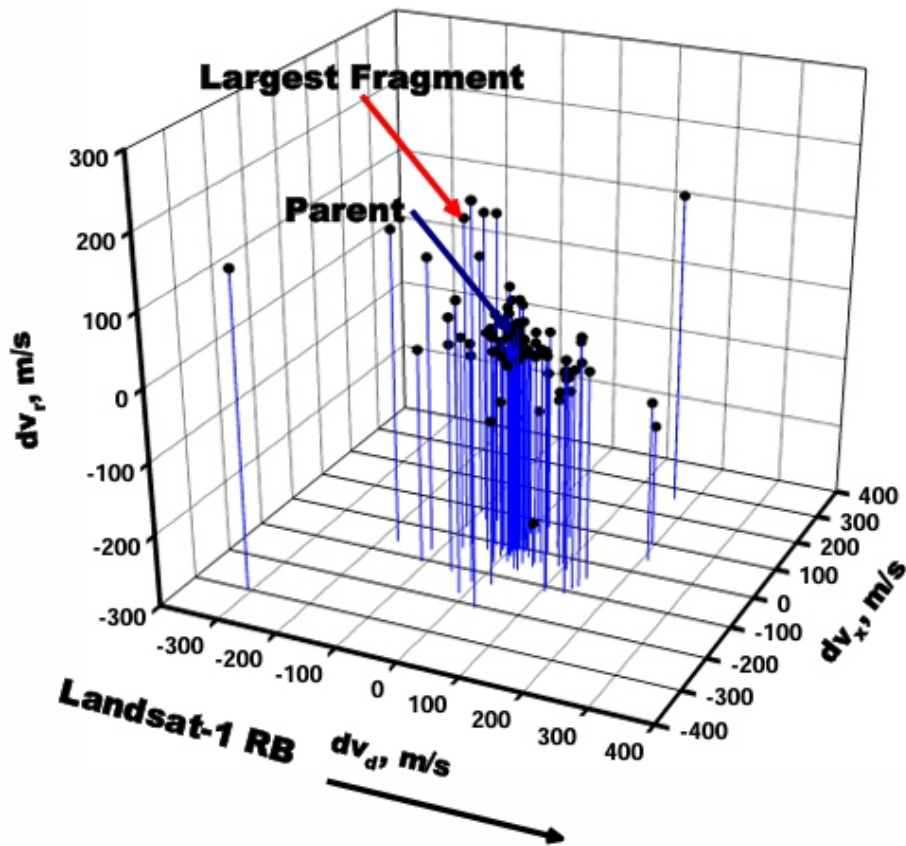


Fig. 4. Three-dimensional scatterplot of velocity perturbation components of Landsat 1 RB fragments.

The first location, by definition, is the origin of the coordinate system. The significantly large displacement of the largest fragment from the origin implies that it had suffered an unusually high velocity perturbation. A noticeably large concentration of fragments on the opposite side of the parent RB suggests that there was a possible recoil effect between these fragments and the largest remnant. A general slope of the fragments towards the positive dv_d and negative dv_x directions is consistent with fragment counts of Table I.

Lastly, we analyze the angular distribution of the Landsat-1 RB fragments. In the local coordinated

system, the latitude λ and longitude ϕ of a fragment are given by:

$$\lambda = \sin^{-1} \frac{dv_r}{dv} \quad (11)$$

and
$$\phi = \tan^{-1} \frac{dv_x}{dv_d} + n\pi \quad (12)$$

where $n = 0$ if $dv_d > 0$; $n = 1$ if $dv_d < 0$ and $dv_x > 0$; and $n = -1$ if $dv_d < 0$ and $dv_x < 0$.

The angular coordinates of the fragments are calculated in accordance with Eqs. (11) and (12) and plotted on a Lambert's equidistant cylindrical projection map (Fig. 5).

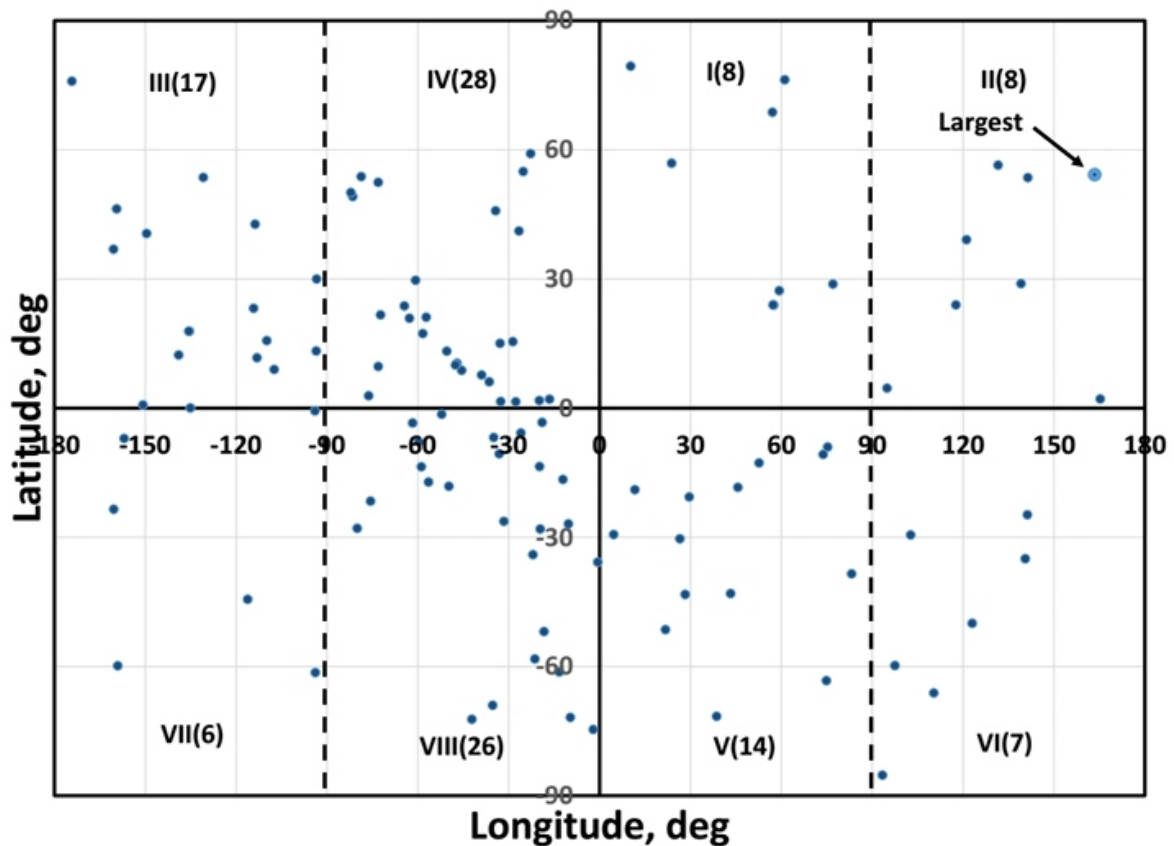


Fig. 5. Angular distribution of fragments of Landsat-1 RB in local frame of reference of the fragmenting parent.

In that map, the latitudes and longitudes are equally spaced. The octants of space are marked together with the number of fragments contained in each octant. The distribution of the fragments were highest in Octants IV and VIII and lowest in Octants I, II and VI. The largest remnant is found in Octant II, one with the fewest fragments, which is diametrically opposite to Octant VIII, one with a large concentration of fragments. Their locations support the suggested recoil effects between the largest

remnant and a large number of fragments in Octant VIII.

DISCUSSION

The explosive fragmentation of the Landsat-1 second stage Delta RB is now analyzed using exact solutions of the fragments' velocity perturbations. Like the NOAA-3 second stage RB fragmentation before it, the roughly Gaussian distribution of the fragments suggests its fragmentation of the RB in the Octant model of the PISCES Code. Unlike the NOAA-3 RB fragmentation, however, the largest remnant of the Landsat-1 RB suffered an unusually large velocity perturbation, which was opposed by the recoil of a large number of fragments found in the diametrically opposite octant of space. It will be interesting to investigate the other Delta stages to have fragmented in orbit for comparison and fuller understanding of the explosive fragmentation of rocket bodies. It will also be instructive to compare with other modes of fragmentation, such as hyper-velocity collision in space [10].

REFERENCES

- [1] R. Dasenbrock, B. Kaufman & W. Heard, *Dynamics of Satellite disintegrations*, NRL Rept. 7964 (1976).
- [2] J.R. Gabbard, *Explosion of Satellite 10704 and other Delta second stage rockets*, NORAD/ADCOM Tech. Memo. 81-5 (1981).
- [3] C.S. Gumpel, *Investigation of Delta second stage on-orbit explosions*, MDC Rept. H0047 (1982).
- [4] G.D. Badhwar, A. Tan, & R.C. Reynolds, *Velocity Perturbations Distributions in the Breakup of Artificial Satellites*, *J. Spacecr. Rockets*, 27, 299-305 (1990).
- [5] N.L. Johnson, E. Stansbery, D.O. Whitlock, K.J. Abercromby & D. Shoots, *History of on-orbit Satellite Fragmentations*, NASA/TM-2008-214779 (2008).
- [6] https://www.space-track.org/perl/id_query.pl
- [7] N.L. Johnson & D.S. McKnight, *Artificial Space Debris*, Orbit Books, Malabar (1987).
- [8] A. Tan, A. Alomari & M. Schamschula, *Analysis of the NOAA-3 rocket fragmentation in orbit using theory and computations*, *Int. J. Aerospace Sci. Applications*, 7, 1 (2017).
- [9] W. Pohl, M.J.V.D. Hoek, J.P. Buis, C.J.L. Florie, S.L. Hancock, P.H.L. Groenenborn, D.J.E. Hesselink & P.J.J. Schaffers, *The PISCES Software for Defence*, PISCES International B.V., The Netherlands (1984).
- [10] A. Tan, F. Allahdadi, S. Maethner & D. Winter, *Satellite Fragmentation: Explosion vs. Collision*, *Orb. Debris. Mon.*, 6(2), 8 (1993).

Velocity Perturbations Analysis of the Fragmentation of USA-193 Satellite in Orbit

Arjun Tan¹ and Robert C. Reynolds²

¹Department of Physics, Alabama A & M University, Normal, AL 35762, U. S. A.
²VVP for Advanced Programs, STAR Dynamics Inc., Hilliard, OH 43026, U.S.A.

ABSTRACT

The radar imaging U.S. military reconnaissance satellite USA-193, launched on 14 December 2006 into a low-Earth orbit, malfunctioned shortly afterwards with its hydrazine propellants unused. In order to mitigate the possible adverse effects of the toxic fuel upon the satellite's atmospheric re-entry, it was destroyed by kinetic impact launched from an SM-3 missile above the Pacific Ocean on 21 February 2008 similar to one conducted in an anti-satellite event. This paper interprets the satellite fragmentation event by calculating and analyzing the velocity perturbations of 170 fragments cataloged through 21.38 days following the breakup. The fragments dispersion was easily the most lopsided and anisotropic amongst all breakup events studied by the authors. The most striking features of the fragment counts are the following: 90% of all fragments were ejected above the horizontal plane; 80% of all fragments were ejected in the forward direction; and an equal number of fragments were ejected to the left and right of the parent satellite when viewed from above. Octant I contained the highest proportion (41%) of the fragments, followed by Octant IV (39%). Thus 80% of all fragments were confined in the two adjacent octants above the horizontal plane. Right below them, no fragments were found in either of Octants V and VIII. Three fragments 32686, 32687 and 32899 with the highest velocity changes were thrown in the negative cross-range direction of the fragmenting satellite. They were recognized as being analogous to the 'anomalous objects' observed in the Solwind P78-1 fragmentation. They also displayed the phenomenon of 'sequential fragmentation' in space. The 'center-of-mass' of the debris cloud was ejected at an amazing speed of 186.67 m/s from the parent, a result never encountered in a satellite breakup before. The small kinetic kill vehicle of the SM-3 missile could not have produced such a debris cloud out of the massive USA-193 satellite by impact alone. The only possible way for this to happen would be for the hydrazine tank to be situated at one end of the satellite and suffer a massive explosion in the 'clam' model of the explosive fragmentation of orbiting propellant tanks.

INTRODUCTION

On 14 December 2006, the radar imaging U.S. military reconnaissance satellite USA193 (International Designator 2006-057A; U.S. Satellite Number 29651) was launched for the National Reconnaissance Office into a low-Earth orbit [1]. The satellite was thought to be 4.6 m long and 2.4 m wide and reportedly weighed about 2,300 kg [2]. It malfunctioned shortly after deployment and as its orbit decayed sufficiently with its hydrazine propellants unused, it was feared that the satellite could survive re-entry into the atmosphere and spew toxic hydrazine into the environment [3]. In order to mitigate this possibility, it was decided to destroy the satellite by kinetic impact in space before its re-entry into the

atmosphere [3]. This happened on 21 February 2008 when a modified SM-3 missile from the U.S. Navy warship Lake Erie struck the satellite over Pacific Ocean at an altitude of 247.769 km, latitude 8.813oN and longitude 189.023oE, thereby thoroughly fragmenting it [1]. The event was reminiscent of the destruction of Solwind P78-1 satellite in 1986 and the Fengyun-1C satellite in 2007 in the anti-satellite tests conducted by the United States of America and People’s Republic of China, respectively. Even though the USA-193 fragmentation was not designated as an antisatellite test, it may not be distinguishable from one. In this paper, we examine the USA-193 fragmentation by (1) examining the Gabbard diagram of the fragments produced; and (2) calculating and analyzing the magnitudes and directions of the fragment velocities. The method of Badhwar, et al. [4] is used for the latter purpose. The orbital elements of USA-193 remain classified, but the relevant information about its last orbit prior to the breakup were calculated from the event location data found in the literature [1]. The data for the orbital elements of the fragments are available from Space-track.org [5].

METHOD OF ANALYSIS

The magnitude, variance and directionality of the ejection velocities of the fragments can shed valuable light regarding the nature and intensity of the fragmentation. Badhwar, et al. [4] obtained exact solutions for the velocity perturbations of the fragments of a breakup. In an orthogonal coordinate system with the fragmenting satellite at the origin and the radial (r), down-range (d) and cross-range (x) directions as the axes, the velocity of the parent satellite at the instance of fragmentation is written as $v_r \hat{r} + v_d \hat{d}$, where

$$v = \sqrt{\mu \left(\frac{2}{r} - \frac{1}{a} \right)} \quad (1)$$

$$v_d = \frac{1}{r} \sqrt{\mu a (1 - e^2)} \quad (2)$$

and

$$v_r = \pm \frac{1}{r} \sqrt{\mu a e^2 - \frac{\mu}{a} (r - a)^2} \quad (3)$$

In Eqs. (1) – (3), a is the semi major-axis and e the eccentricity of orbit; r is the radial distance from the center of the Earth; and μ is the gravitational parameter of the Earth. In Eq. (3), the + sign corresponds to the ascending mode of the satellite (true anomaly $\theta < \pi$) whereas the – sign corresponds to the descending mode ($\theta > \pi$).

Upon fragmentation, the velocity of a fragment has the components $v_r + dv_r$, $v_d + dv_d$ and dv_x , with dv_r , dv_d and dv_x being the velocity perturbation components of the fragment [4]:

$$dv_r = \pm \sqrt{\mu \left(\frac{2}{r} - \frac{1}{a'} \right) - \frac{\mu}{r^2} a' (1 - e'^2)} - v_r \quad (4)$$

$$dv_d = \frac{\cos \xi}{r} \sqrt{\mu a' (1 - e'^2)} - v_d \quad (5)$$

and

$$dv_x = \frac{\sin \xi}{r} \sqrt{\mu a' (1 - e'^2)} \quad (6)$$

In Eq. (4), the + sign corresponds to the ascending mode of the fragment (true anomaly $\theta' < \pi$), whereas the – sign corresponds to the descending mode ($\theta' > \pi$).

In Eqs. (5) and (6), ξ is the plane-change angle of the fragment given by [4]:

$$\xi = \pm \cos^{-1} \frac{\cos i \cos i' + \sqrt{\cos^2 \lambda - \cos^2 i} \sqrt{\cos^2 \lambda - \cos^2 i'}}{\cos^2 \lambda} \quad (7)$$

where λ is the latitude of the fragmentation point. In Eq. (7), the + sign corresponds to $i' > i$ and the – sign corresponds to $i' < i$ on the northbound orbits with the opposite sense on the southbound orbits, i and i' being the inclinations of the parent and fragment, respectively.

The true anomaly θ' of the fragment, which dictates the sign of dv_r , is determined from the argument of latitude u' and the argument of perigee ω' of the fragment at the time of the breakup as: $\theta' = u' - \omega'$. Since the argument of perigee is perturbed by the oblateness of the Earth, the argument of perigee at the time of observation ω_0' is different from its value at the time of fragmentation ω' . From the rate of precession, one has [6]:

$$\omega' = \omega_0' - 4.98 \left(\frac{R}{a} \right)^{7/2} \frac{5 \cos^2 i - 1}{(1 - e'^2)^2} dt \quad (8)$$

where R is the reference radius of the Earth (6,378.137 km), dt is the time of observation from the time of fragmentation in days, and ω' and ω_0' are expressed in degrees.

The velocity perturbation components dv_d , dv_x and dv_r may be used to define various planes and quarters of space. For example, dv_d and dv_x define the local horizontal plane; and dv_r , and dv_d define a vertical plane which is the plane of the orbit. dv_r , and dv_x define the other vertical plane perpendicular to the plane of the orbit. Two angular coordinates are defined as follows: (1) the **latitude** λ , measured from the horizontal plane; and (2) the **longitude** ϕ , measured from the plane of the orbit:

$$\lambda = \sin^{-1} \left(\frac{dv_r}{dv} \right) \quad (9)$$

and

$$\phi = \tan^{-1} \left(\frac{dv_x}{dv_d} \right) + n\pi \quad (10)$$

where $n = 0$ if $dv_d > 0$; $n = 1$ if $dv_d < 0$ and $dv_x > 0$; and $n = -1$ if $dv_d < 0$ and $dv_x < 0$. λ ranges from $-\pi/2$ to $\pi/2$; whereas ϕ ranges from $-\pi$ to π . The eight octants of space are defined in accordance to the scheme indicated in Table I.

Table I. Fragment counts in various quarters of space					
Fragments in regions of space	dv_d	dv_x	dv_r	Count	%
Fragments in all space	all	all	all	170	100
Fragments ejected upwards	all	all	+	153	90
Fragments ejected downwards	all	all	-	17	10
Fragments ejected forwards	+	all	all	136	80
Fragments ejected backwards	-	all	all	34	20
Fragments ejected to the left*	all	+	all	85	50
Fragments ejected to the right*	all	-	all	85	50
Fragments ejected in Octant I	+	+	+	69	41
Fragments ejected in Octant II	-	+	+	10	6
Fragments ejected in Octant III	-	-	+	7	4
Fragments ejected in Octant IV	+	-	+	67	39
Fragments ejected in Octant V	+	+	-	0	0
Fragments ejected in Octant VI	-	+	-	6	4
Fragments ejected in Octant VII	-	-	-	11	6
Fragments ejected in Octant VIII	+	-	-	0	0
*looking downwards from the parent satellite at fragmentation					

RESULTS

The orbital elements of USA-193 remain classified as of now. However, its last orbit prior to impact can be constructed from bits of data found in the open literature. For example, we have: the apogee height $h_a = 257$ km; perigee height $h_p = 241$ km; inclination $i = 58.48^\circ$ [7]; and event date and time, 21 February 2008 0326 GMT [1]. From the basic equations of the orbital ellipse, one gets: $a = 6,627.645$ km; $e = .001131624$; and true anomaly $\theta = 76.7189^\circ$ (ascending mode); whence by Eqs. (1) – (3): $v = 7.757166447$ km/s; $vd = 7.757161747$ km/s; and $vr = 8.53952$ m/s.

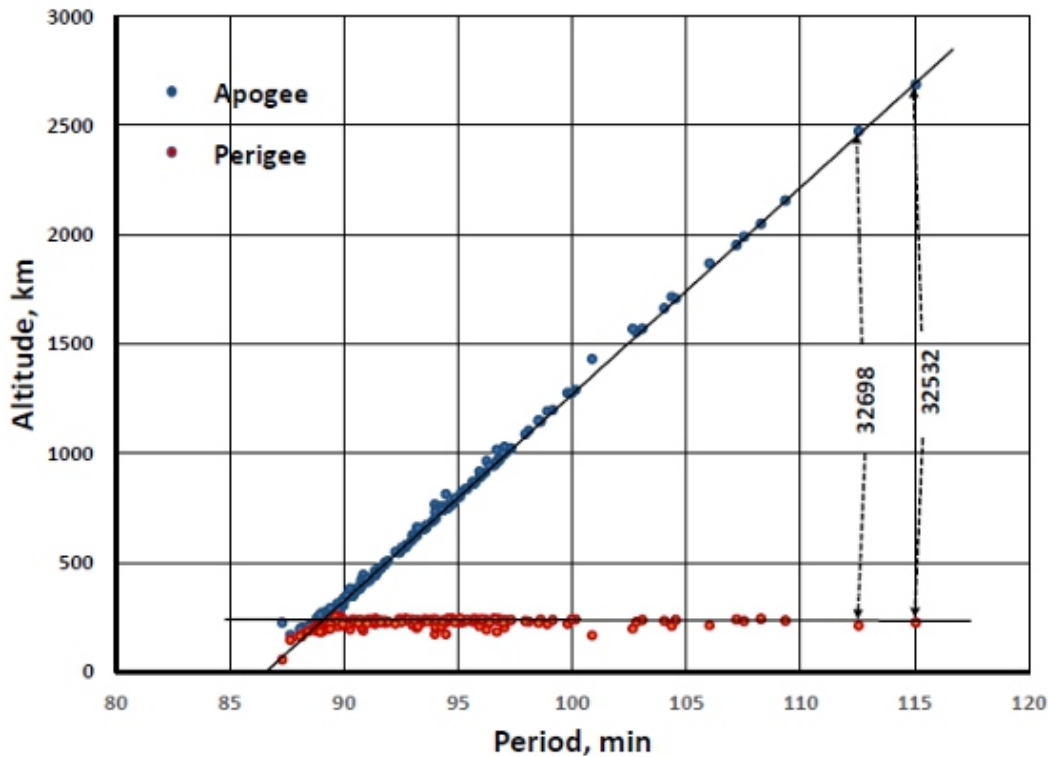


Fig. 1

Figure 1 is the Gabbard diagram of 170 fragments of USA-193 cataloged through 21.38 days following the breakup. During that period, 203 fragments (serial numbers 32502 consecutively through 32704) were urgently tracked, out of which 170 were cataloged, the rest presumably having de-orbited early. The Gabbard diagram plots the apogee and perigee heights (h_a and h_p , respectively) of each fragment against its orbital period P . For a breakup occurring in a nearly circular orbit at a relatively low altitude, the typical Gabbard diagram shows an inclined 'X' form, with its left arms largely missing and acquiring a 'claw shape'. In this case, the left arms are almost completely missing, whereby suggesting that most of the fragments with negative dvd 's had deorbited rapidly. The two fragments on the far right (32698 and 32532) on the other end received the highest dvd 's in the positive down-range direction. The fragments dispersion in the USA-193 breakup event was easily the most lopsided and anisotropic amongst all breakup events studied by the authors. The fragment counts in the various quarters of space are compiled in Table I. The most striking features of the fragment counts are the following: (1) 90% of all fragments were ejected above the horizontal plane and the remainder 10% below it; (2) 80% of all fragments were ejected in the forward direction and only 20% in the retrograde direction; and (3) An equal number of fragments were ejected to the left and right of the parent satellite when viewed from above. Octant I contained the highest proportion (41%) of the fragments, followed by Octant IV (39%). Thus 80% of all fragments were confined in the two adjacent octants above the horizontal plane. Right below them, no fragments were found in either of Octants V and VIII.

	dv_d , m/s	dv_x , m/s	dv_r , m/s	dv , m/s
Maximum	572.68	279.73	340.04	942.56
Minimum	-121.73	-941.25	-8.54	18.81
Average	106.62	-22.49	76.35	186.67
Range	694.41	1,220.98	348.58	923.75

Table II shows the highest, lowest and average values of the dv_d , dv_x , dv_r and dv and their ranges. The large positive average values of dv_d and dv_r confirm the fact that most of the fragments were ejected in the forward and upward directions. The unusually wide range of the dv_x values were due to three fragments (32686, 32687 and 32899), reminiscent of the three ‘anomalous objects’ observed in the Solwind P78-1 fragmentation [8], which were later recognized as ‘ricochet fragments’ produced by hypervelocity impact [9]. These three fragments had the highest ejection speeds amongst all fragments (Table III, which also includes the next seven fragments). However, unlike the Solwind anomalous objects, they do not stand out in the Gabbard diagram like the fragments 32532 and 32698 (Fig. 1), which had the next highest dv values (Table III). The reason for this is that their dv_d values were negative, which did not act in enhancing their orbital periods.

Fragment #	dv_d , m/s	dv_x , m/s	dv_r , m/s	dv , m/s
32686	-49.01	-941.25	-8.54	942.56
32687	-53.00	-940.94	-8.54	942.47
32699	-121.73	-933.81	-8.54	941.75
32532	572.68	4.54	236.13	619.47
32698	525.21	-59.11	296.68	606.10
32583	467.84	92.70	162.92	504.00
32591	430.68	158.15	172.03	400.00
32502	282.10	-176.42	340.04	475.75
32503	399.11	-27.27	252.85	473.25
32597	448.50	28.80	94.56	459.26

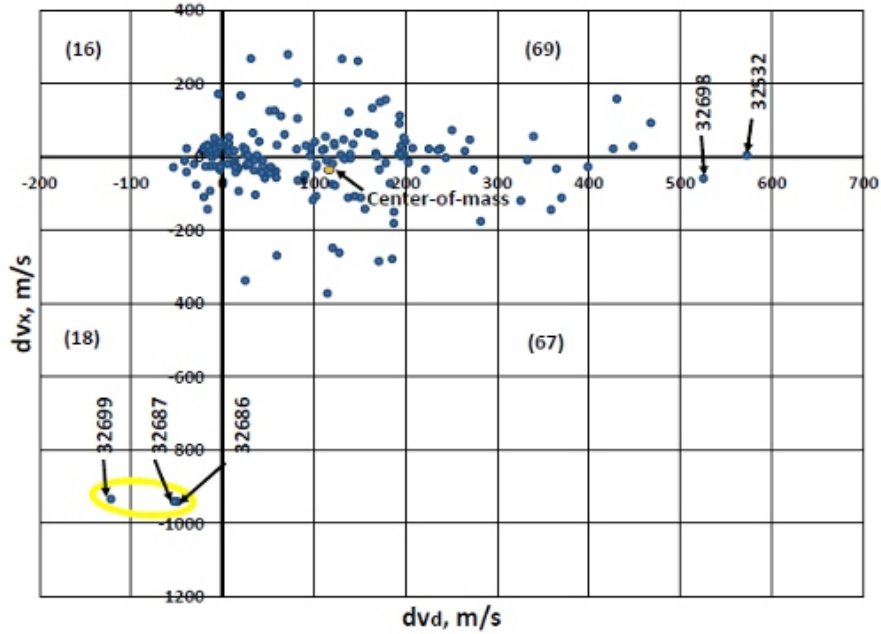


Fig. 2

Figure 2 is a scatterplot of the fragments in the horizontal dv_x – dvd plane as viewed from above. Fragments having the largest dvd 's (32698 and 32532) are marked on the far right. The fragments 32699, 32687 and 32686 having the highest dv 's are shown on the lower left corner. They were ejected to the far right of the fragmenting satellite path seen from above. Also shown in the figure is the 'center-of-mas' having the average dv values, i.e., with each fragment weighted equally. Since all fragments were reportedly small ('not larger than an American football') [2], this characterization is not an unfair one. The numbers of fragments in each quadrant of space are marked in Fig. 2. Clearly, the first and fourth quadrants contained the vast majority of the fragments.

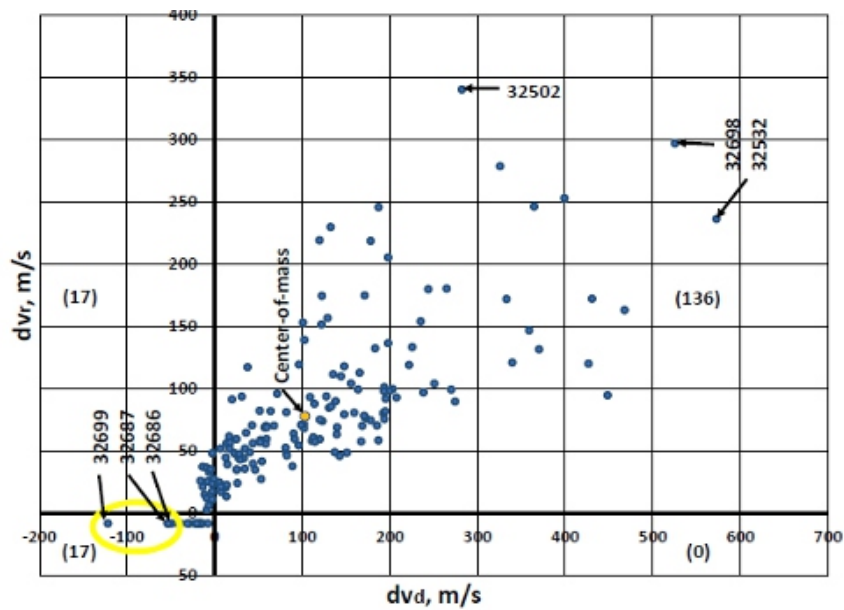


Fig. 3

Figure 3 is a scatterplot of the fragments in a vertical plane containing the orbit of the fragmenting satellite, which is the dvr – dvd plane. The fragments 32698 and 32532 take their prominent places in the first quadrant which contains an astonishing 136 out of 170 (or 80%) of all fragments. The anomalous fragments (32699, 32687 and 32686) take a lowly backseat in the third quadrant, on the verge of imminent re-entry into the atmosphere. The slope of the center-of-mass of the fragments in this dvr – dvd orbital plane is a steep (vide Table II) $\tan^{-1}(76.35/106.62) = 35.6^\circ$. The actual slope of the center-of-mass cloud from the horizontal plane is, however (from Eq. 9) $\sin^{-1}(76.35/186.67) = 24.14^\circ$. The latter angle is suggestive of the slope of the interceptor when it hit its target.

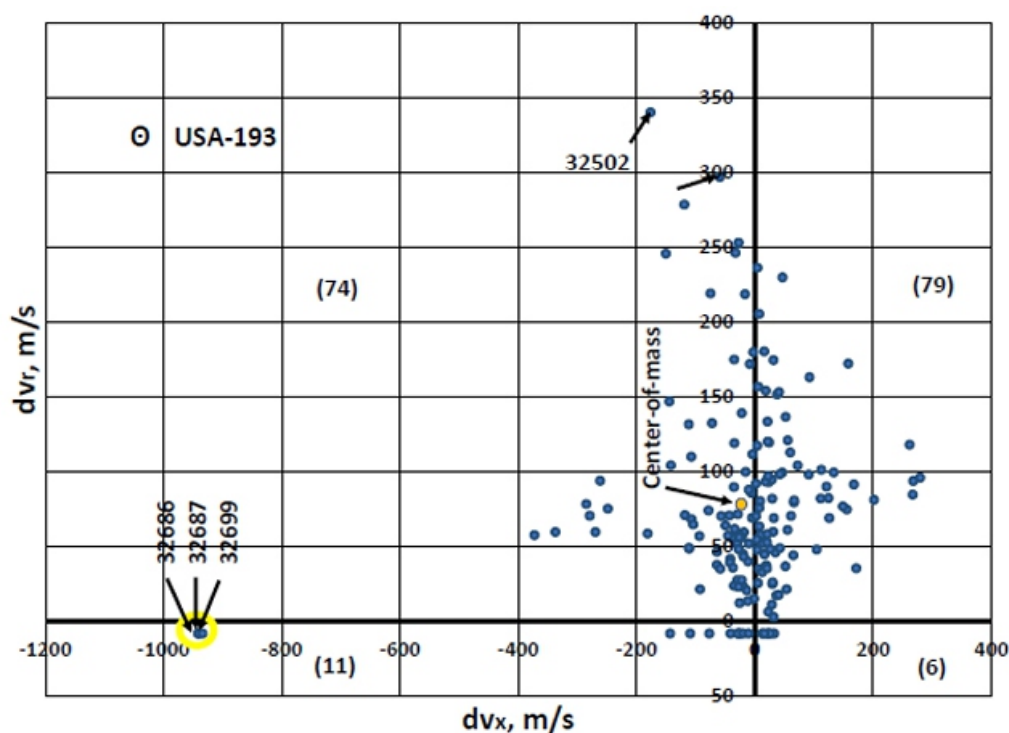


Fig. 4

Figure 4 is the scatterplot of the fragments in a second vertical plane containing the orbital angular momentum vector of the fragmenting satellite, which is the dvr – $d vx$ plane. Its features are consistent with those of Figs. 2 and 3. The direction of the parent satellite is vertically out of the plane. A full 90% of the fragments were found in the first two quadrants, with a slightly higher number in the first quadrant (79) than in the second (74). However, the center-of-mass of the fragments was slightly inside the latter quadrant, due perhaps to the three anomalous fragments far flung to the left. These fragments are now bunched tightly together, unlike in Figs. 2 and 3, where there was a substantial gap between 32699 on one hand and 32686 and 32687 on the other. This may well be a classic example of sequential fragmentation in space, first proposed by Brown [10] and later observed by Tan, et al. [9] in the Solwind

P78-1 fragmentation by kinetic impact. The likely scenario played out is as follows: A large chunk of fragment breaks out off the target, which first fragments into two pieces, one fragment 32699 and the other still a composite of 32686 and 32687; and the latter subsequently undergoing a second fragmentation into 32686 and 32687.

The angular distributions of the USA-193 fragments are shown on Lambert's equidistant cylindrical projection map in Fig. 5. The numbers of fragments in each of the eight octants are marked. Most fragments were found in Octant I (69 or 41%) followed by in Octant IV (67 or 39%) with the two octants accounting for 80% of the fragments. Right below them, there were no fragments in octants V and VIII. Overall, there were 153 fragments (90%) above the horizontal plane and only 17 (10%) below the horizontal plane. The three anomalous fragments with the highest velocity changes (32686, 32687 and 32699) are bunched together near the four corners of Octants III, IV, VII and VIII. The fragment with highest dvr (32502) is marked on the map as well as the fragment with the second highest dvd (32698). Not far from the latter is located the center-of-mass of all fragments.

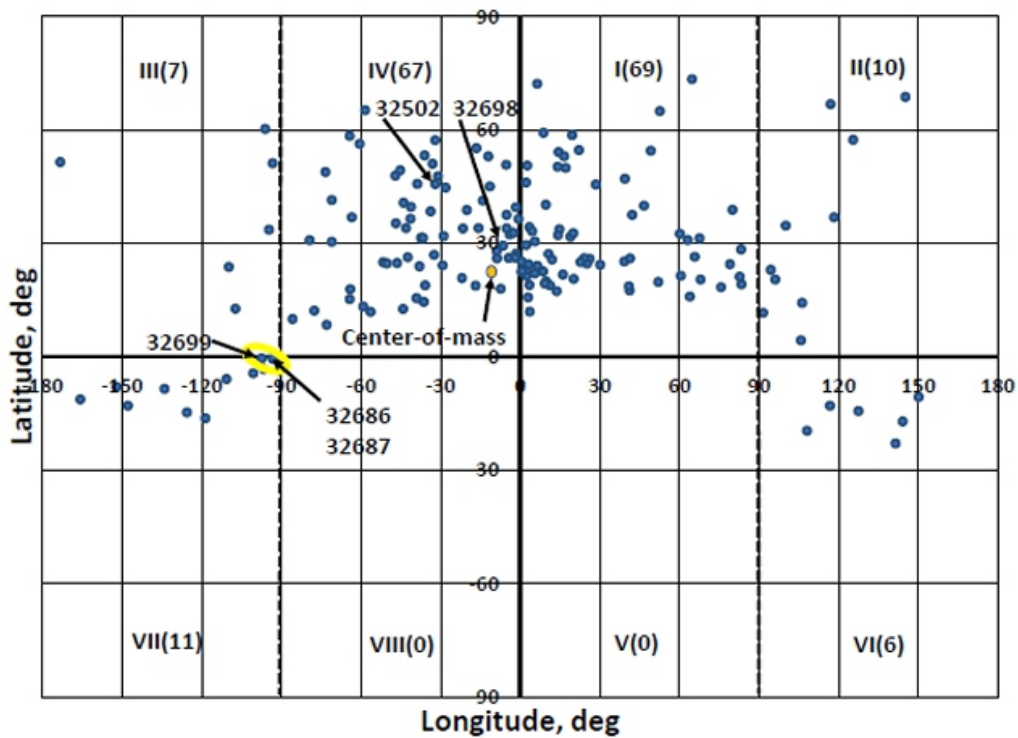


Fig. 5

DISCUSSION

The fragmentation of USA-193 by kinetic impact is like no other satellite fragmentation on record. With 90% of the fragments moving above the horizontal plane, 80% of the fragments moving the forward direction, and the center-of-mass of the cloud moving at an amazing speed of 186.67 m/s, this

fragmentation is in a class by itself. The small kinetic kill vehicle of the SM-3 missile (LEAP) could not have produced such a debris cloud out of the massive USA-193 satellite by impact alone [11]. The only possible way for this to happen will be for the hydrazine tank to be situated at one end of the satellite and suffer a massive explosion in the ‘clam model’ of the explosive fragmentation of orbiting propellant tanks [12].

REFERENCES

- [1] P. Anz-Meador, J.N. Opiela, D. Shoots & J.-C. Liou, *History of on-orbit Satellite Fragmentation*, NASA/TM-2018-22037 (2018), p. 458.
- [2] <https://celestrak.com/events/usa-193.php>.
- [3] *Orbital Debris Quarterly News*, 12(2), 1-2 (2008).
- [4] G.D. Badhwar, A. Tan, & R.C. Reynolds, *Velocity Perturbations Distributions in the Breakup of Artificial Satellites*, *J. Spacecr. Rockets*, 27, 299-305 (1990).
- [5] https://www.space-track.org/perl/id_query.pl
- [6] D. King-Hele, *Satellite Orbits in an Atmosphere*, Blackie (Glasgow, 1987), p.6.
- [7] <https://en.wikipedia.org/wiki/USA-193>.
- [8] R. Kling, *Postmortem of a hypervelocity impact*, *Teledyne Brown Engineering Rept. CS86-LKD-001* (1986).
- [9] A. Tan, G.D. Badhwar, F.A. Allahdadi & D.F. Medina, *Analysis of the Solwind fragmentation using theory and computations*, *J. Spacecr. Rockets*, 33, 79-85 (1996).
- [10] W.K. Brown, *A theory of sequential fragmentation and its astrophysical applications*, *J. Astrophys. Astronom.*, 10, 89-112 (1989).
- [11] http://web.mit.edu/stgs/pdfs/Forden_Preliminary_analysis_USA_193_Shoot_down.pdf.
- [12] F.J. Benz, R.L. Kays, C.V. Bishop & M.B. Eck, *Explosive fragmentation of orbiting propellant tanks in Orbital Debris from Upper Stage Breakup*, J.P. Loftus ed., AIAA, Washington (1989), pp. 107-129.

Posthumous Analysis of the Indian Anti-Satellite Experiment Part III: A Plausible Fragmentation Scenario

Arjun Tan

Department of Physics, Alabama A & M University, Normal, AL 35762, U. S. A.

ABSTRACT

The Indian anti-satellite (ASAT) experiment of 27 March 2019 created several unexpected results. The most unusual amongst them was that the Gabbard diagram was that of four separate fragmentations, the first of its kind ever recorded. The primary fragmentation was caused by the hypervelocity impact of the ASAT, which was followed by three successive explosive fragmentations of the main remnant of the target satellite. The fragments produced by each breakup was characterized by its apogee and perigee lines of definite slopes. A theory of apsidal slopes is formulated which shows that the sum of the slopes of the apogee and perigee lines is a constant for fragmentation from any location in the same orbit. The slopes of the apsidal lines were calculated at various true anomalies of the fragmenting orbit and compared with the observed slopes. The true anomalies of the breakup locations were determined where the calculated values of the slopes matched the observed values. It was concluded without ambiguity that the explosions occurred at 1-minute intervals at true anomalies of 93o, 97o and 101o in the ascending phase in a remnant orbit, 0.12404 day or approximately two revolutions after the initial collision of the ASAT with its target. The dramatic increases in the size and ellipticity of the remnant orbit following the explosions support these findings.

I. INTRODUCTION

On 27 March 2019, India became the fourth nation in history to attain anti-satellite (ASAT) capability when its Microsat-R satellite was destroyed in Sun-synchronous orbit. The ASAT weapon was a kinetic kill vehicle (KKV) atop a third-stage rocket launched from Abdul Kalam Island [1]. The impact occurred at 11:13 IST or 05:43 UT on Julian day 2019086 at epoch 2019086.23819444. The location of the event was over Bay of Bengal at 18.715oN latitude and 87.450oE longitude [2]. The mass of the target satellite was 740 kg whereas the third-stage rocket including the KKV weighed 1,800 kg [3]. The ASAT experiment was planned such that the fragments produced by the backward impulse would deorbit rapidly and pose no threat to the space environment. However, several hundreds of fragments spread in the forward direction, many of them into higher energy orbits. By the end of the year 2019, 348 fragments (excluding the main remnant of the parent satellite) were cataloged [4]. Analyses of this event showed that the breakup of the Microsat-R satellite was one of a unique kind never witnessed before [5, 6]. The Gabbard diagram of the fragments revealed that it comprised four distinct Gabbard diagrams belonging to four groups of fragments in one, each having its own apogee and perigee lines, which was possible only if four distinct fragmentations had taken place sequentially [5]. The slopes of the apsidal lines together with the epochs of the fragments first cataloged point to the following

scenario: The primary fragmentation was caused by the hypervelocity impact of the KKV producing Group 1 fragments; which was followed by the secondary, tertiary and quaternary fragmentations caused by explosions in the main remnant of the target satellite in rapid successions, producing fragment Groups 2, 3 and 4 [5]. Of the 348 cataloged fragments, 144 belonged to Group 1 and the rest 204 belonged to the latter groups [5]. The fragments of the latter groups were so tightly clustered together that numerical breakdown of them was not feasible. Figure 1 shows the composite Gabbard diagram with the apogee and perigee lines of the Group 1 fragments marked. Figure 2 shows only the Groups 2, 3 and 4 fragments with their respective apsidal lines, with the Group 1 fragments purged (for better clarity). The observed slopes of the apogee and perigee lines were calculated graphically and entered in Table I. In this paper, a theory of apsidal line slopes is formulated and compared with the observed slopes. The details of the sequence of four fragmentations are extracted from the results,

Table I. Observed Slopes of Apsidal Lines in Gabbard Diagram			
Fragments Group	Apogee Line Slope	Perigee Line Slope	Sum of Apsidal Lines Slopes
Group 1 Fragments	93.06 km/min	0.31 km/min	93.38 km/min
Group 2 Fragments	49.07 km/min	45.00 km/min	94.07 km/min
Group 3 Fragments	53.69 km/min	41.38 km/min	95.07 km/min
Group 4 Fragments	56.86 km/min	38.53 km/min	95.39 km/min

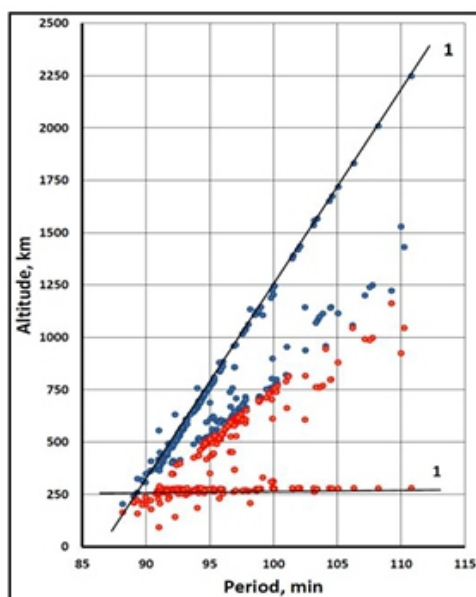


Fig. 1

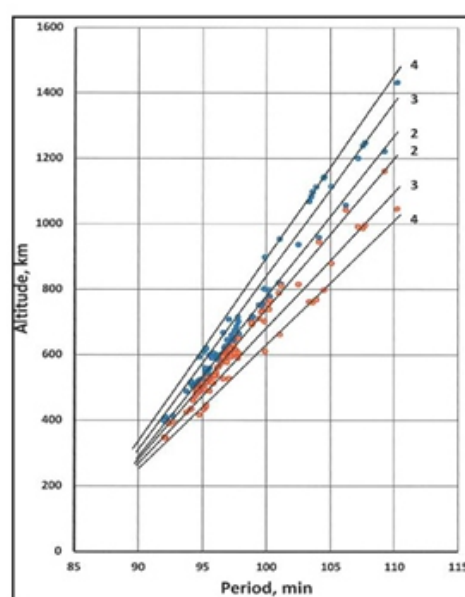


Fig. 2

2. THEORY OF APSIDAL LINES FORMATION ON GABBARD DIAGRAM

The Gabbard diagram of the fragments of a breakup event is a plot of the apogee and perigee heights of the fragments against their orbital time periods. Of the three orthogonal velocity perturbation components of a fragment dv_r , dv_d and dv_x in the radial, down-range and cross-range directions respectively, only the first two are relevant in this diagram. The apogee and perigee lines in the Gabbard diagram are produced by dv_d s only, with the dv_r s producing departures of the points from these lines [7]. The change in apogee and perigee heights of a fragment, dh_A and dh_P respectively, are given by:

$$dh_A = \frac{1+e}{n} \left[2(1 + e \cos \theta) + \frac{(1-e) \cos \theta (2+e \cos \theta)}{1+e \cos \theta} \right] dv_d \quad (1)$$

and

$$dh_P = \frac{1-e}{n} \left[2(1 + e \cos \theta) - \frac{(1+e) \cos \theta (2+e \cos \theta)}{1+e \cos \theta} \right] dv_d \quad (2)$$

where e is the eccentricity of the fragmenting orbit, n the mean motion and θ is the true anomaly. To evaluate the slopes of the apogee and perigee lines, dh_A/dP and dh_P/dP respectively, in the Gabbard diagram, one needs to convert dv_d to the period P of the fragmenting orbit. This process consists of several steps:

First, for small eccentricities ($e \leq .01$), the **change in energy of a fragment** dE is overwhelmingly due to dv_d [7]:

$$dE = v_d dv_d \quad (3)$$

Second, the change in energy dE is associated with the **change in period** dP :

$$dE = -\frac{2E}{3P} dP \quad (4)$$

Third, the energy of the orbit is:

$$E = -\frac{\mu}{2a} \quad (5)$$

where μ is the **gravitational parameter of the Earth** and a is the **semi-major axis of the fragmenting orbit**.

Fourth, convert the mean motion n into the **orbital time period** P via the defining equation:

$$n = \frac{2\pi}{P} \quad (6)$$

Substituting Eqs. (3) – (6) into Eqs. (1) and (2) and simplifying, we obtain the intermediate forms for the slopes of the apogee and perigee lines:

$$\frac{dh_A}{dP} = \frac{\mu}{6\pi av_d} (1 + e) \left[2(1 + e \cos\theta) + \frac{(1-e)\cos\theta(2+e\cos\theta)}{1+e\cos\theta} \right] \quad (7)$$

and

$$\frac{dh_P}{dP} = \frac{\mu}{6\pi av_d} (1 - e) \left[2(1 + e \cos\theta) - \frac{(1+e)\cos\theta(2+e\cos\theta)}{1+e\cos\theta} \right] \quad (8)$$

Finally, we extricate the θ -dependence in v_d from its expression and the equation of the orbit:

$$v_d = \frac{\sqrt{\mu(1-e^2)}}{r} \quad (9)$$

and

$$r = \frac{a(1-e^2)}{1+e\cos\theta} \quad (10)$$

to obtain:

$$\frac{dh_A}{dP} = \frac{1}{6\pi} \sqrt{\frac{\mu(1-e^2)}{a}} \left[2(1 + e) + \frac{(1-e^2)\cos\theta(2+e\cos\theta)}{(1+e\cos\theta)^2} \right] \quad (11)$$

and

$$\frac{dh_P}{dP} = \frac{1}{6\pi} \sqrt{\frac{\mu(1-e^2)}{a}} \left[2(1 - e) - \frac{(1-e^2)\cos\theta(2+e\cos\theta)}{(1+e\cos\theta)^2} \right] \quad (12)$$

In Eqs. (9) – (12), r stands for the **radial distance of the fragmentation point from the center of the Earth**.

Summing Eqs. (7) and (8), and simplifying, one gets:

$$\frac{dh_A}{dP} + \frac{dh_P}{dP} = \frac{1}{6\pi} \sqrt{\frac{\mu(1-e^2)}{a}} \quad (13)$$

Eq. (13) implies that the sum of the slopes of the apsidal lines is constant for any orbit of definite size (a) and shape (e) and is independent of the true anomaly θ , where the fragmentation took place. Stated alternatively, we have a theorem of conservation of slopes of the apsidal lines which states that the sum of the slopes of the apsidal lines is constant regardless of where the fragmentation takes places from the same orbit. It should be noted that according to Eqs. (11) and (12), the perigee line slope dh_P/dP is minimum when the true anomaly $\theta = 0$. As θ increases, dh_P/dP increases and dh_A/dP decreases. At some point, the two slopes become equal and after that the two lines are interchanged. In general, the angle between the two lines is maximum near the apogee ($\theta = 0$) and perigee ($\theta = \pi$) and zero near $\theta = \pi/2$ and $\theta = 3\pi/2$.

3. BREAKUP JOURNEY OF MICROSAT-R TARGET SATELLITE

Prima facie evidence suggests that Microsat-R, the target satellite of the Indian ASAT experiment, suffered four distinct fragmentations. Immediately prior to the hypervelocity impact with the ASAT, it was found in a nearly circular orbit of eccentricity $e = .0015984$, henceforth called Orbit 1. After the collision which produced the Group 1 fragments, the largest remnant, which inherited the identity of the target satellite, was found in a smaller, but slightly more elliptical orbit ($e = .0028309$), now referred to as Orbit 2. It is in this orbit that the Microsat-R remnant may well have undergone three successive explosive breakups caused by the ignition of residual propellants in the satellite, which produced fragment Groups 2, 3 and 4 [5]. After an interval of several days, the Microsat-R remnant was cataloged in Orbit 3 with the highest apogee height and greatest eccentricity of its lifetime ($e = .0101419$). The relevant orbital parameters of the three reference orbits are listed in Table II, which will prove to be crucial in our following analysis.

Table II. Relevant Pre- and Post-Breakup Orbits of Microsat-R				
Orbit	Epoch, day	Eccentricity	Semi-major axis, km	Period, min
Orbit 1	86.19975	.0015984	6,649.061	89.92904
Orbit 2	86.32379	.0028309	6,645.465	89.85610
Orbit 3	95.00724	.0101419	6,659.421	90.13930

The velocity perturbation components dv_d and dv_r which took Microsat-R from Orbit 1 to Orbit 2 are given, respectively, by [7]:

$$dv_d = \frac{na\sqrt{1-e^2}}{2r} \left(da - \frac{2ae}{1-e^2} de \right) \quad (14)$$

and

$$dv_r = \frac{na^2\sqrt{1-e^2}}{2er^2\sin\theta} \left[2aede - \left(1 - e^2 - \frac{r^2}{a^2} \right) da \right] \quad (15)$$

where n is the mean motion of the fragmenting satellite. In terms of the number of revolutions per day N (loosely called its namesake):

$$n = \frac{2\pi N}{24 \times 60 \times 60} \quad (16)$$

From the value of $N = 16.01262446$ [4], Eq. (16) furnishes: $n = .001164471/s$. The value of r at the fragmentation point in Orbit 1 is calculated to be 6,659.046431 km [5]. Also, the true anomaly of the target satellite at impact is estimated to be $\theta = 160.03260$ [5]. The changes in semi-major axis da and eccentricity de from Orbit 1 to Orbit 2 (from Table II) provide: $dv_d = -2.10592$ m/s; and $dv_r = 16.35609$ m/s. These values are qualitatively consistent with the head-on impact with the KKV from below the horizontal plane [5]. As a result of the first breakup of the target satellite by impact, its remnant was found in a smaller and lower orbit (due to retrograde dv_d) with a higher eccentricity (due to positive dv_r).

4. CALCULATED SLOPES OF THE APSIDAL LINES

Since all the relevant quantities in Eqs. (11) and (12) are known for Orbits 1 and 2, the slopes of the apogee and perigee lines of the Group 1 fragments can be calculated directly from these two equations. At the instant of collision, the true anomaly of Microsat-R was 160.03260 and the height of the breakup was 280.9014 km [5]. The results for the Group 1 fragments: $dv_A/dP = 95.76$ km/min; $dv_P/dP = 2.95$ km/min. These values compare favorably with the observed slopes of Group 1 apsidal lines (Table I). For the explosive breakups from Orbit 2, the true anomaly is unknown. In order to find this, we calculate the change in true anomaly from Orbit 1 to Orbit 2 (cf. [8]):

$$d\theta = \frac{\sqrt{1-e^2}}{nae} \left[\cos\theta dv_r - \sin\theta \left(1 + \frac{1}{1+e\cos\theta} \right) dv_d \right] \quad (17)$$

getting $d\theta = -64.525380$; whence the true anomaly for Orbit 3: $\theta' = \theta + d\theta = 95.50740$. The slopes of the apogee and perigee lines were next calculated for Orbit 2 at intervals of 10 true anomaly. As noted earlier, the slopes depended exclusively on the true anomaly, with their sum remaining constant. Table III covers selected ranges in which the results match with the observed slopes for the Group 2, 3 and 4 lines shown in Table I. By inspection, there were two ranges where this was realized: one for ascending motion; and the other for descending motion of the fragmenting Microsat-R remnant. For ascending motion, the calculated slopes matched the observed slopes for the Group 2, 3 and 4 lines for true anomalies of 930, 970 and 1010 respectively (marked yellow in Table III); whereas for descending motion, this happened at true anomalies of 2730, 2770 and 2810 respectively (marked yellow in Table III), at diametrically opposite ends of the orbit. Since the estimated true anomaly for Orbit 2 was 95.50, it is concluded without any ambiguity that the explosive fragmentations which produced fragment Groups 2, 3 and 4 must have taken place during the ascending motion of the Microsat-R remnant in Orbit 2. One can bolster this conclusion from the perturbations of the semi-major axis da and eccentricity de of Orbit 2 prescribed by Lagrange's planetary equations (cf. [8]):

$$da = \frac{2}{n} \left[\frac{e \sin \theta}{\sqrt{1-e^2}} dv_r + \frac{a\sqrt{1-e^2}}{r} dv_d \right] \quad (18)$$

and

$$de = \frac{\sqrt{1-e^2}}{na} \left\{ \sin \theta dv_r + \left[\frac{a(1-e^2)}{er} - \frac{r}{ae} \right] dv_d \right\} \quad (19)$$

Equations (18) and (19) indicate that the effects of dv_r were to increase or decrease both da and de for ascending ($0 < \theta < \pi$) or descending ($\pi < \theta < 2\pi$) motions, respectively.

Table III. Calculated Slopes of Apsidal Lines for Group 2, 3, 4 Fragments				
Sense of Motion	θ , deg	dh_A/dP , km/min	dh_P/dP , km/min	$(dh_A+dh_P)/dP$, km/min
Ascending	92	50.89	47.72	98.61
	93	51.75	46.82	98.61
	94	52.61	45.00	98.61
	95	53.46	45.15	98.61
	96	54.32	44.29	98.61
	97	55.18	43.43	98.61
	98	56.03	42.58	98.61
	99	56.88	41.73	98.61
	100	57.73	40.88	98.61
	101	58.58	40.03	98.61
	102	59.42	39.18	98.61
Descending	272	51.16	47.44	98.61
	273	52.02	46.58	98.61
	274	52.88	45.73	98.61
	275	53.74	44.87	98.61
	276	54.60	44.01	98.61
	277	55.45	43.16	98.61
	278	56.30	42.31	98.61
	279	57.15	41.46	98.61
	280	58.00	40.61	98.61
	281	58.84	39.76	98.61
	282	59.69	38.92	98.61

In fact, the changes are maximum at $\theta = 90^\circ$ and minimum at $\theta = 270^\circ$. The dramatic increases in both da and de from Orbit 2 to Orbit 3 favor the ascending phase of the remnant's motion.

As Orbit 2 was still fairly circular ($e = .0022976$) having an orbital period of around 90 min., the 40 intervals between two consecutive explosions translate to 1 min. each for the time intervals, which means that the three explosions were over in the space of 2 minutes. The time interval between the first and second fragmentations, by contrast, as calculated from the epochs of Orbits 1 and 2, translate to 0.12404 d. = 178.62 min. or 2 revolutions. In summary, the explosive fragmentations which produced fragment Groups 2, 3 and 4 took place at true anomalies of 93° , 97° and 101° respectively in rapid succession of 1 min. intervals after approximately 2 revolutions in the remnant's orbit.

5. CONCLUSION

Our earlier studies had shed considerable light on various puzzles surrounding the Indian ASAT experiment involving the target satellite Microsat-R [5, 6]. For examples, why was hypervelocity impact not sufficient in explaining the observed debris production; and why explosive fragmentations of the surviving remnant must have taken place in order to explain the observed Gabbard diagram of the fragments. This study reinforces the findings of our earlier studies [5, 6] and gives a plausible chronological scenario of the subsequent explosions consistent with the slopes of the apsidal lines in the Gabbard diagram and pinpoints the locations of the exploding remnant in its breakup orbit.

REFERENCES

- [1] https://wikipedia.org/wiki/Mission_Shakti.
- [2] <https://thediplomat.com/2019/05/why-indias-asat-test-was-reckless>.
- [3] <http://indiandefensenews.in/2019/04/all-you-need-to-know-about-pdv-mkii/html>.
- [4] <https://www.space-track.org>.
- [5] A. Tan, R.C. Reynolds & R. Ramachandran, *Posthumous analysis of the Indian anti-satellite experiment: Puzzles and Answers*, *Adv. Aerospace Sci. Appl.*, 10, 1, 2020.
- [6] A. Tan, R.C. Reynolds & R. Ramachandran, *Posthumous analysis of the Indian anti-satellite experiment, Part II: Fragment dispersion study*, *Adv. Aerospace Sci. Appl.*, 10, 11, 2020.
- [7] A. Tan & R.C. Reynolds, *Theory of Satellite Fragmentation in Orbit*, *WorldScientific* (2020).
- [8] L. Meirovitch, *Methods of Analytical Dynamics*, *McGraw-Hill*, New York (1970).

Investigating the YunHai 1-02 Satellite Fragmentation using Theory and Velocity Perturbations Analysis of its Fragments

Arjun Tan

Department of Physics, Alabama A & M University, Normal, AL 35762, U. S. A.

ABSTRACT

The fragmentation of YunHai meteorological satellite in an accidental collision with a small orbital debris in orbit is investigated in this paper. First, the twoline orbital element (TLE) sets of the two colliding satellites prior to the collision as well as those of the 45 fragments following the collision are gathered from the Space-track website available to the public. All the quantities required for this study are derived and propagated to the time of collision. The ground tracks of YunHai and the debris in the final pass are determined, and the angle and relative collisional speed calculated using spherical trigonometry. The Gabbard diagram of the fragments exhibited large drag effects, suggesting the possibility that a solar panel of YunHai was struck by the debris. Velocity perturbations of the fragments were calculated using exact solutions in the three orthogonal components in the fragmenting satellite's frame of reference. Scatterplot in the horizontal plane shows that the fragments spread was more or less isotropic, but a significantly more fragments with greater spread velocities were located in a quadrant in the direction of the incoming debris. The velocity perturbations in the radial direction were mostly indeterminate due to the strong drag effects. An interesting cross-quadrant distribution of fragments was noticed in a vertical plane containing the orbit of the fragmenting satellite.

INTRODUCTION

On 18 March 2021, the operational Chinese meteorological satellite YunHai 1-02 (International designator 2019-063A; Catalog number 44547) fragmented in a Sun-synchronous orbit [1]. The cause of this fragmentation was assessed to be an accidental collision with a small mission-related debris (International designator 1996-051Q; Catalog number 48078) associated with the SL-16 launch vehicle for the deployment of Cosmos 2333 satellite [2]. YunHai 1-02 was reported to be partially operational after the impact, raising speculation that the debris may have hit one of its solar panels [3].

Figure 1 (courtesy of T.S. Kelso [4]) shows that the collision occurred above the tip of the Scandinavian peninsula at 70°N latitude and 19°E longitude [4]. At encounter, YunHai was southbound whereas the debris was approaching its northernmost point in orbit [4]. This study analyzes the geometrical and dynamical aspects of this collision by calculating the relative velocity of encounter between YunHai and the fragment, and the velocity perturbations received by the fragments of collision.



Figure 1

ORBITAL ELEMENTS OF YUNHAI AND DEBRIS AT ENCOUNTER

The historical orbital elements of all orbiting satellites in the form of two-line element sets (TLEs) are archived in the web [5]. For YunHai, the latest TLEs prior to the breakup is obviously chosen. For the debris, the lone TLE set found in the archive is chosen by default. The quantities inputted directly are universal time (epoch) of the breakup t ; inclination i ; eccentricity e ; right ascension of ascending node (RAAN) Ω ; argument of perigee ω ; mean anomaly M ; and mean motion (revolutions per day) n . The following quantities are derived from the above: semi-major axis a ; period P ; apogee height h_a and perigee height h_p . The true anomaly θ which marks the position of a satellite in its orbit is calculated from the mean anomaly M via the eccentric anomaly E from the standard equations. These quantities for YunHai and the debris are calculated from the latest TLEs at epoch t prior to the breakup and entered in Table I. Next, the quantities at the time of collision (epoch t_0) are calculated. The Earth's oblateness causes changes in the orbital elements ω and Ω (called the J_2 -effect). The respective changes $d\omega$ and $d\Omega$ are calculated using the expressions of King-Hele [6] and the arguments of perigee (ω_0) and RAANs (Ω_0) at collision determined, with the latter marking the locations of the ascending nodes. The descending nodes are located at the anti-podal points diametrically opposite to the ascending nodes. The right ascensions of the descending nodes (RADN) are obtained by adding or subtracting 180° to or from RAAN, respectively. The true anomaly of YunHai at collision θ_0 is obtained by adding $d\theta$ calculated from dM via dE whereas the true anomaly of the debris is obtained from the equation of the

orbit, whence the arguments of latitude u_0 are determined and entered in Table I.

Table I. Orbital Elements of YunHai Satellite and Rocket Debris prior to and at Encounter

Parameter	Symbol	YunHai	Debris
International designator		2019-063A	1996-051Q
US Catalog Number		44547	48078
Epoch prior to collision	t	21077.29960554	21075.18227694
Inclination	i	98.5408°	71.0590°
Eccentricity	e	.0003532	.0132231
Mean motion	n	14.32749197/day	14.14595323/day
Semi-major axis	a	7160.6961 km	7221.8292 km
Period	P	100.5061 min	101.7959 min
Apogee height	h_a	785.0803 km	939.1792 km
Perigee height	h_p	780.0220 km	748.1893 km
Argument of perigee	ω	110.1122°	41.5133°
RA of ascending node	Ω	105.1634°	233.6196°
Mean anomaly	M	250.0437°	319.5940°
Eccentric anomaly	E	250.0247°	319.0930°
True anomaly	θ	250.0057°	318.5944°
Epoch at collision	t_0	21077.3201388	21077.3201388
Interval from t to t_0	dt	0.02053326 d	2.13786186 d
Change in ω after dt	$d\omega$	-0.0607°	-3.2639°
Change in Ω after dt	$d\Omega$	-0.0228°	-4.4779°
Argument of perigee at t_0	ω_0	110.0515°	38.2494°
RAAN at t_0	Ω_0	105/465.1397°	228.8409°
RADN at t_0	$\Omega_0 \pm \pi$	285.1397°	48/409.8409°
Change in M after dt	dM	107.1029°	-
Change in E after dt	dE	108.0586°	-
Change in θ after dt	$d\theta$	108.0779°	-
True anomaly at t_0	θ_0	358.0835°	48.7397°
Argument of latitude at t_0	u_0	108.1351°	86.9891°

ENCOUNTER GEOMETRY AND DYNAMICS

YunHai was in retrograde Sun-synchronous orbit ($i = 98.5408^\circ$) whereas the debris was in prograde orbit ($i = 71.0590^\circ$). The orbit of YunHai was nearly circular ($e = .0003432$) while that of the debris was slightly more elliptical ($e = .0132231$). Their apsidal heights (Table I) indicate that collision was possible only in a narrow altitude range between 780 km and 785 km. The radial distance of the fragmentation point from the center of the Earth r is estimated from the equation of orbit, giving $r = 7158.166968$ km; whence the altitude of fragmentation $h = r - r_\oplus = 780.02197$ km, $r_\oplus = 6378.137$ km being the reference radius of the Earth.

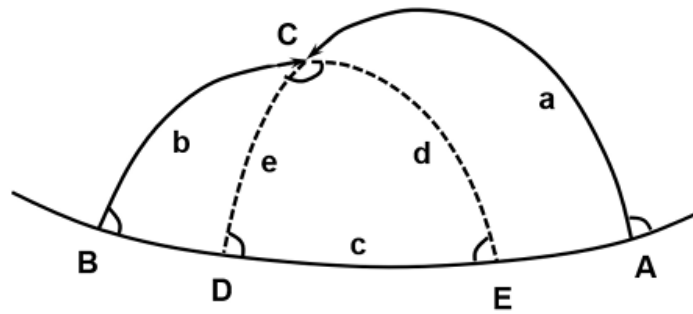


Figure 2

Figure 2 is a schematic diagram of the encounter of YunHai with the debris. In that figure, ACD is the ground-track of YunHai; BCE that of the debris; and AEDB marks the equator. All three are great circles and thus the laws of spherical trigonometry apply here. The angles at the equator are related to the inclinations of the orbits: $\angle A = 98.5408^\circ$; $\angle B = \angle E = 71.0590^\circ$; and $\angle D = 180^\circ - 98.5408^\circ = 81.4592^\circ$. Angles a , b , c , d and e are defined at the center of the Earth of which $\angle a$, $\angle b$, $\angle d$ and $\angle e$ are related to the arguments of latitudes of YunHai and the debris: $\angle a = 108.1351^\circ$; $\angle b = 86.9891^\circ$; $\angle d = 180^\circ - \angle b = 93.0109^\circ$; and $\angle e = 180^\circ - \angle a = 71.8649^\circ$. Lastly, $\angle c$ is equal to the difference between the two RADNs: $\angle c = 124.7012^\circ$.

The angle of encounter $\angle C$ can be determined from the spherical triangle CDE. From the law of sines, we have [7]:

$$\frac{\sin C}{\sin c} = \frac{\sin A}{\sin a} = \frac{\sin B}{\sin b} \quad (1)$$

Equation (1) constitutes three equations, only two of which are independent. The lefthand side equation yields the value of $\angle C = 54.9113^\circ$ or $180^\circ - 54.9113^\circ = 125.0887^\circ$. By inspection, the first solution is deemed to be extraneous, which gives for the angle of encounter: $\angle C = 125.0887^\circ$. The right-hand side equation gives the same results. In the frame of reference of YunHai looking vertically downwards, the debris came from the right with a large head-on component. Also, YunHai was travelling nearly

horizontally, whereas the debris was ascending, as indicated by their true anomalies at t_0 .

Finally, the orbital speeds of YunHai and the fragment at collision are calculated from the traditional vis-viva equation. We get at the encounter point: the speed of Yunhai $v_s = 7.4635$ km/s; and that of the debris $v_d = 7.4950$ km/s. The relative speed of encounter between the two is given by the equation:

$$v_{sd} = \sqrt{v_s^2 + v_d^2 - 2v_s v_d \cos C} \quad (2)$$

Upon substituting values, we get: $v_{sd} = 13.2738$ km/s. This is by far the highest relative speed of encounter between any two colliding objects in orbit recorded thus far, surpassing the collision speed of 11.57 km/s between Iridium 33 and Cosmos 2251 satellites in February 2009 [8].

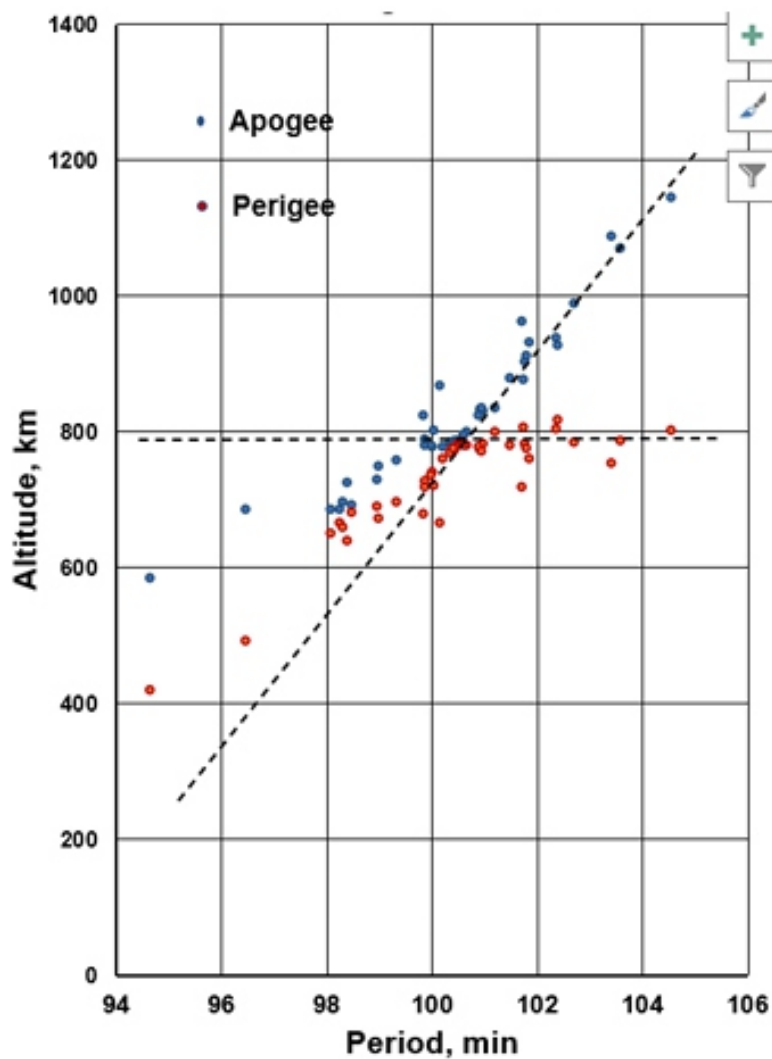


Figure 3

GABBARD DIAGRAM OF YUNHAI FRAGMENTS

The Gabbard diagram is one of the oldest investigative tools in a satellite fragmentation study. It is a plot of the apogee and perigee heights of the fragments as functions of their periods. The Gabbard diagram

has distinguishing patterns depending upon the eccentricity of the fragmenting satellite's orbit and its true anomaly at the point of fragmentation which therefore can shed light regarding the breakup. For a nearly circular orbit such as YunHai's, the Gabbard diagram resembles an inclined 'X' form, with fragments lying above and below the arms of the X. When pristine, i.e., taken immediately upon breakup, the angles between the arms are devoid of fragments. Air drag soon moves fragments into the 'forbidden zone', especially on the left-hand side. Figure 3 is the Gabbard diagram of 45 YunHai fragments archived through day 271 of 2021. As is seen, migrating fragments have populated the entire forbidden zone on the left-hand side, indicating stronger drag forces than usual for a breakup at 780 km altitude. This tends to support the notion that the fragments came from the flat solar panels, bolstering the suspicion that the debris hit a solar panel rather than the main body of the satellite.

VELOCITY PERTURBATIONS OF THE YUNHAI FRAGMENTS

The magnitude, variance and directionality of the ejection velocities of the fragments can shed valuable light regarding the nature and intensity of the fragmentation. Badhwar, et al. [9] obtained exact solutions for the velocity perturbations of the fragments of a breakup. In an orthogonal coordinate system with the fragmenting satellite at the origin and the radial (®), down-range (d) and cross-range (x) directions as the axes, the velocity of the parent satellite at the instance of fragmentation is written

as $\vec{v} = v_r \hat{r} + v_d \hat{d}$, where

$$v_d = \frac{1}{r} \sqrt{\mu a (1 - e^2)} \quad (3)$$

and

$$v_r = \pm \frac{1}{r} \sqrt{\mu a e^2 - \frac{\mu}{a} (r - a)^2} \quad (4)$$

with μ being the *gravitational parameter of the Earth*. In Eq. (4), the + sign corresponds to the *ascending mode* of the satellite whereas the – sign corresponds to the *descending mode*.

Upon fragmentation, the velocity of a fragment has the components $v_r + dv_r$, $v_d + dv_d$ and dv_x , where the *velocity perturbation components of the fragment* are in the three orthogonal directions are given by [9]:

$$dv_r = \pm \sqrt{\mu \left(\frac{2}{r} - \frac{1}{r'} \right) - \frac{\mu a'}{r^2} (1 - e'^2)} - v_r \quad (5)$$

$$dv_d = \frac{\cos \zeta}{r} \sqrt{\mu a' (1 - e'^2)} - v_d \quad (6)$$

and

$$dv_x = \frac{\sin \zeta}{r} \sqrt{\mu a' (1 - e'^2)} \quad (7)$$

In the above equations, the primed quantities pertain to the fragment's orbit, and λ is the plane change angle of the fragment's orbit from the parent's orbit. In Eq. (5), the + sign corresponds to the ascending mode of the fragment and the – sign corresponds to the descending mode. The plane change angle λ is calculated from the inclinations of the parent's and fragment's orbits and the latitude of the breakup point λ as:

$$\zeta = \pm \cos^{-1} \frac{\cos i \cos i' + \sqrt{(\cos^2 \lambda - \cos^2 i)(\cos^2 \lambda - \cos^2 i')}}{\cos^2 \lambda} \quad (8)$$

Here the + sign corresponds to $i' > i$ and the – sign corresponds to $i' < i$ on the **northbound orbits** with the opposite sense on the **southbound orbits**.

Table II gives a summary of the velocity perturbations (dv_r , dv_d and dv_x), their ranges, frequencies and counts. Also entered in the table are the **total perturbation speeds** $dv = \sqrt{dv_r^2 + dv_d^2 + dv_x^2}$ and **kinetic energy perturbations** $\frac{1}{2}dv^2$ as a result. The dv_d s were slightly more numerous in the negative direction (25) than in the positive (20). For the dv_x s, the results were exactly opposite (20 to 25). In the radial direction, over half (25) of the dv_r s calculations were **indeterminate**. This is owing to the fact that due to the high drag effects, the orbits of the parent and the fragment no longer intersected when the earliest TLEs were archived. As is customary, the dv_r s in such cases were forced equal to zeros.

Table II. Velocity perturbations of the YunHai Fragments and Fragment Counts

	dv_d , m/s	dv_x , m/s	dv_r , m/s	dv , m/s	$\frac{1}{2}dv^2$, m ² /s ²
Maximum	96.82	171.18	38.39	228.07	26,007.39
Minimum	-150.71	-163.72	-111.14	0.78	0.31
Average	-2.96	13.06	-9.01	63.59	3,699.13
Range	247.53	334.89	149.53	227.28	26,007.08
Positive count	20	25	8	45	45
Negative count	25	20	12	0	0
Indeterminate	0	0	25	–	–
Total count	45	45	45	45	45

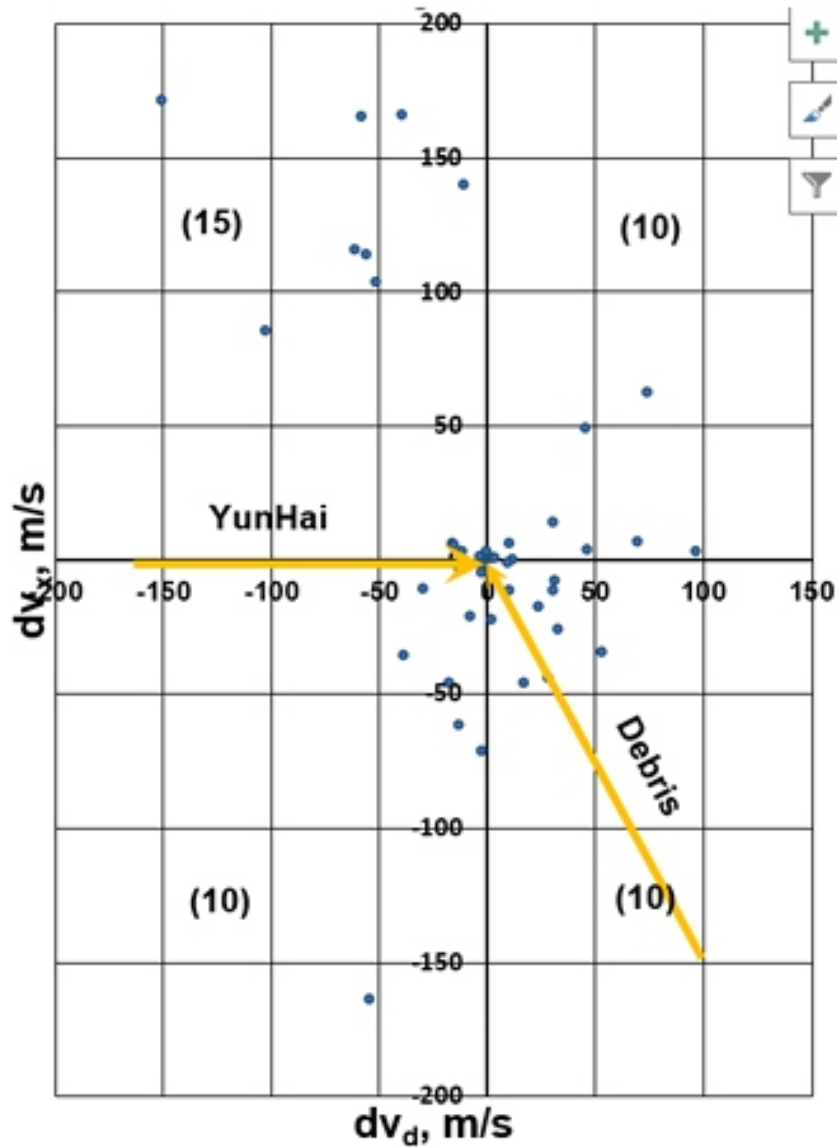


Figure 4

Figure 4 is a scatterplot of the YunHai fragments in the local horizontal plane at the breakup point. The directions of the colliding objects are marked in this figure. Overall, the fragment scatter is roughly isotropic, with equal number of fragments (10) in each of the quadrants I, III and IV. Only quadrant II had more fragments (15), which also were scattered farther in general. Whether this can be interpreted as due to momentum transfer from the impacting debris cannot be ruled out. On the other hand, it cannot be taken for confirmed because of the sample size of the data.

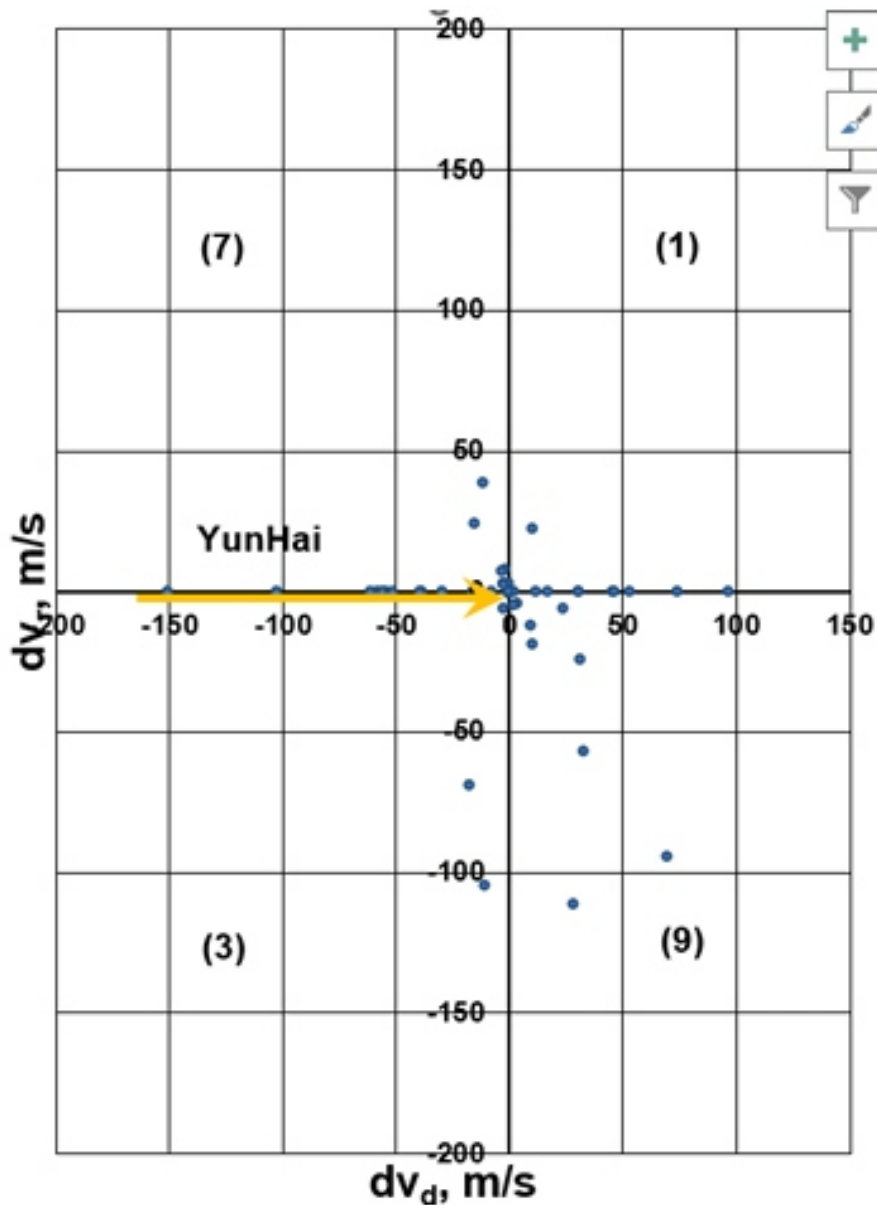


Figure 5

Figure 5 is a scatterplot of the YunHai fragments in a local vertical plane containing the orbital plane of the fragmenting satellite. The path of YunHai is marked in that figure as well as the fragment counts in each quadrant. The total fragment counts in the four quadrants add up to only 20. The remaining 25 of the cataloged fragments had indeterminate dv_r s and are shown as situated on the dv_d axis. The real scenario cannot be reconstructed unless the TLEs of all fragments are known immediately upon formation. Only interesting observation is noted in Fig. 5. A vast majority of 16 fragments out of 20 are found in the cross-quadrants of II and IV; and the rest (4 fragments) are located in the other cross-quadrants of I and III.

REMARKS

The breakup of YunHai spacecraft marks the fourth time in history when an orbiting satellite was accidentally hit by a small object which was either a mission-related debris or a fragmentation debris [2]. In all the previous cases, the number of cataloged fragments was a small single-digit figure. However, in this case, at least 45 fragments of the collision were cataloged. This places the YunHai fragmentation event in a separate category of its own.

REFERENCES

- [1] *Orbital Debris Quarterly News*, 25 (2), June 2021.
- [2] *Orbital Debris Quarterly News*, 25 (4), December 2021.
- [3] <https://space.com/space-junk-collision-chinese-satellite-yunhai-1-02>.
- [4] ts.kelso@celestrak.com.
- [5] <https://www.space-track.org>.
- [6] D. King-Hele, *Satellite Orbits in an Atmosphere*, Blackie (Glasgow, 1987).
- [7] cf. F. Ayres, *Theory and problems of Spherical Trigonometry*, Schaum Publ., New York (1954).
- [8] cf. A. Tan, T.X. Zhang & M. Dokhanian, *Adv. Aerospace Sci. Appl.*, 1, 13-25 (2013).
- [9] G.D. Badhwar, A. Tan, & R.C. Reynolds, *J. Spacecr. Rockets*, 27, 299-305 (1990).

Investigating Russia's Direct-Ascent Anti-Satellite Test

Arjun Tan

Department of Physics, Alabama A & M University, Normal, AL 35762, U. S. A.

ABSTRACT

Russia's direct-ascent anti-satellite (ASAT) test on its Cosmos 1408 satellite on 15 November 2021 is investigated in this paper by analyzing the orbital elements of the fragments produced and also calculating the velocity perturbations and angular distribution of the fragments. This test differed from the ASAT tests of the United States, China and India of the past in at least two distinct ways. First, the Russian ASAT actually attained orbital trajectory prior to the impact; and second, the Russian ASAT hit its target generally from behind instead of from the side or almost head-on. Consequently, a distinct ASAT cloud was produced, not witnessed in the earlier ASAT tests. Besides the ASAT cloud, high-energy 'ricochet fragments' were produced similar to those observed in the Solwind breakup event and the Delta-180 collision experiment in space. The angle of encounter between the target and the ASAT was calculated from which the condition of ricochet formation was seen to be met. The fragments spread in the orbital plane displayed a beautiful 'butterfly pattern' seen before only in the Ariane rocket fragmentation event. If the latter breakup was indeed caused by an orbital debris, then the formation of a butterfly pattern constitutes a second 'sufficient condition for collision in space'. Finally, the angular distribution of the fragments was obtained on an equidistant cylindrical projection map. There was a major concentration area in the fifth octant of space extending into the sixth octant south of the local horizontal plane.

INTRODUCTION

The first nation to successfully launch an artificial satellite – the former Soviet Union, was also the first nation to successfully conduct an anti-satellite (ASAT) test against an orbiting satellite. On 1 November 1968, an interceptor satellite (also referred to as killer or hunter satellite) Cosmos 252 was launched into a coplanar orbit of the target satellite Cosmos 248 and maneuvered into a rendezvous point where the perigee of the interceptor and the apogee of the target satellite coincided, whereupon the former was exploded on command, producing fragments, one of which impacting the latter and destroying it [1–3]. The first direct-ascent anti-satellite test was conducted by the United States on 13 September 1985 against its Solwind P78-1 satellite [4–6]. On that day, a two-stage rocket was launched from an F-15 Eagle jet fighter which upon burnout, released a miniature homing vehicle (MHV), which in turn, guided by infra-red sensors and steering jets, converged on its target, destroying it thoroughly [4–6]. On 11 January 2007, the People's Republic of China attained its ASAT capability when its target satellite

Fengyun-1C was destroyed by a kinetic kill-vehicle (KKV) launched from a two-stage ballistic missile [7, 8]. This ASAT test was reminiscent of the U.S. ASAT experiment of 1985. In both cases, the ASAT projectiles hit their targets from the side. On 27 March 2019, India became the third nation to demonstrate the direct-ascent ASAT capability when its Microsat-R satellite was destroyed by a KKV atop a third-stage rocket launched from Abdul Kalam Island [9, 10]. The KKV was joined to the third-stage rocket when it hit the target from a nearly head-on direction.

Obviously, the direct-ascent ASAT is far superior to the now obsolete Soviet-era coorbital ASAT method because of its direct approach to the target satellite and far shorter flight path and consequently shorter time of flight to its destination. Hence, for Russian Federation, the successor state to the former Soviet Union, to repeat the ASAT tests of the USA, China and India would not make much sense reputationally. Rather, it was compelling for Russia to demonstrate something newer and more effective version of a direct-ascent ASAT test. This actually happened on 15 November 2021 when Russia's A-235 Nudol ASAT missile destroyed its defunct reconnaissance satellite Cosmos1408 (International Designator 1982-092A, U.S. Catalog Number 13552) at 0250 UT above 75°N latitude; 60°E longitude; and 485 km altitude [11–14]. Unlike the U.S., Chinese and Indian ASAT tests, the Russian ASAT hit its target generally from behind and thus retained some essential features of the Soviet-era co-orbital ASAT method [13, 14]. Chasing a target from behind requires greater speed vis-à-vis the earlier direct-ascent ASAT tests where the ASAT hit the target from the side or from the front. It also meant that the Russian ASAT had to enter into an orbital trajectory rather than using a sub-orbital trajectory which was sufficient for the earlier direct-ascent ASAT tests. In this paper, we investigate Russia's own direct-ascent ASAT test by analyzing the orbital elements of the fragments produced, their Gabbard diagram, and the calculated velocity perturbations of the fragments.

HYPERVELOCITY COLLISIONAL PHENOMENOLOGY IN SPACE

Our knowledge of hypervelocity collisional phenomenology in orbital space was largely learnt from two landmark experiments in space: (1) The fragmentation of the Solwind P78-1 satellite in the U.S. ASAT experiment mentioned earlier; and (2) The Delta-180 collision experiment by the U.S. Strategic Defense Initiative Organization on 5 September 1986. In the latter experiment, the payload of a Delta 180 launch vehicle was made to collide with its second stage rocket [16, 17]. The results of the Solwind ASAT test revealed for the first time that high-energy fragments can be produced when a projectile hits the target satellite in orbit [4–6]. These high-energy fragments have now been identified as ricochet fragments produced by oblique impact of the projectile on its target [6, 18]. The condition of ricochet formation has been established as follows: the angle of incidence of the projectile I has to be at least 45°,

whence the angle of reflection of the ricochet R is 79° or greater. so that $I + R$ has to be at least 124° [6, 18]. Since ricochet fragments are not produced in explosive fragmentation of orbiting satellites, this condition has been referred to as a sufficient (but not necessary) condition for collisional fragmentation in orbit [18].

The results of the Delta-180 experiment have shown that when two large objects collide in orbit, each object produces its own debris cloud centered around its orbiting center-of-mass as if it fragmented on its own, i.e., without any momentum transfer from the other fragmenting object [16, 17]. A far smaller number of fragments follow their own orbits separate from the two dominant debris clouds [16, 17]. It is the latter fragments which had suffered from momentum transfer and originated near a small contact region between the two colliding objects. It is also the latter fragments to which the ricochet fragments necessarily belong [6, 18].

ORBITAL ELEMENTS STUDY OF THE FRAGMENTS

Prior to the breakup, Cosmos 1408 was in a nearly circular orbit having an inclination of 82.5637° , eccentricity .001857 and mean motion of 15.29390138, which translates to a period of 94.15517756 min, apogee height of 490.360 km and perigee height of 464.898 km [15]. Shortly after the event, the Global Space Surveillance Network of the U.S. Space Force detected over 1,500 trackable fragments, making it the third highest fragment-producing event in history [11]. By the end of 2021, the orbital elements of 946 fragments were cataloged in the Space-Track.org website [15], with this number growing to 1,865 by Day 216 of 2022.

A preliminary inspection of the orbital elements of the cataloged fragments reveals that the vast majority of the fragments' inclinations centered around (82.58°), which is nearly the same as the inclination of Cosmos 1408 (82.56°) prior to collision. These fragments therefore constitute the target cloud. However, most surprisingly, a small but significant number (75) of fragments having inclinations around 87.4° formed a separate cloud, which must now be identified as the ASAT cloud. This is a new development, since in the earlier direct-ascent ASAT experiments, the MHV or KKV's traversed sub-orbital trajectories and therefore the ASAT clouds formed quickly deorbited. This indicates that the Nudol ASAT must have entered orbital trajectory prior to the impact. Further, most of the fragments of ASAT cloud had small eccentricities similar to that of the target satellite which indicates that their orbits were also quite circular like the target's orbit. This is possible if the ASAT itself was in a nearly circular orbit prior to impact. Consequently, the whole collision event can fairly be visualized on the local horizontal plane containing the encounter point.

A closer inspection of the orbital elements data reveals that 21 fragments in the target cloud (U.S. Serial Numbers 49924–49944) were ejected into higher energy orbits, which present themselves as potential candidate for ricochet fragments. In order to explore this possibility, we calculate the angles between (1) the target satellite

(inclination $i_1 = 82.5637^\circ$), (2) ASAT fragments (average inclination $i_2 = 87.3997^\circ$) and (3) the energetic fragments (average inclination $i_3 = 82.5181^\circ$). The angle of encounter ζ between two orbiting satellites having inclinations i_1 and i_2 at a latitude λ is shown to be [19]:

$$\zeta_{12} = \pm \cos^{-1} \frac{\cos i_1 \cos i_2 + \sqrt{(\cos^2 \lambda - \cos^2 i_1)(\cos^2 \lambda - \cos^2 i_2)}}{\cos^2 \lambda} \quad (1)$$

Given $\lambda = 75^\circ$, we get: $\zeta_{12} = 19.9081^\circ$ and $\zeta_{13} = .2018^\circ$; whence, $\zeta_{23} = \zeta_{12} + \zeta_{13} = 20.1099^\circ$ (vide Fig. 1). Then the angle $I + R$ of our previous discussion is $180^\circ - \zeta_{23} = 159.8901^\circ > 124^\circ$. Hence the *energetic fragments indeed satisfy the sufficient condition to be ricochet fragments*.

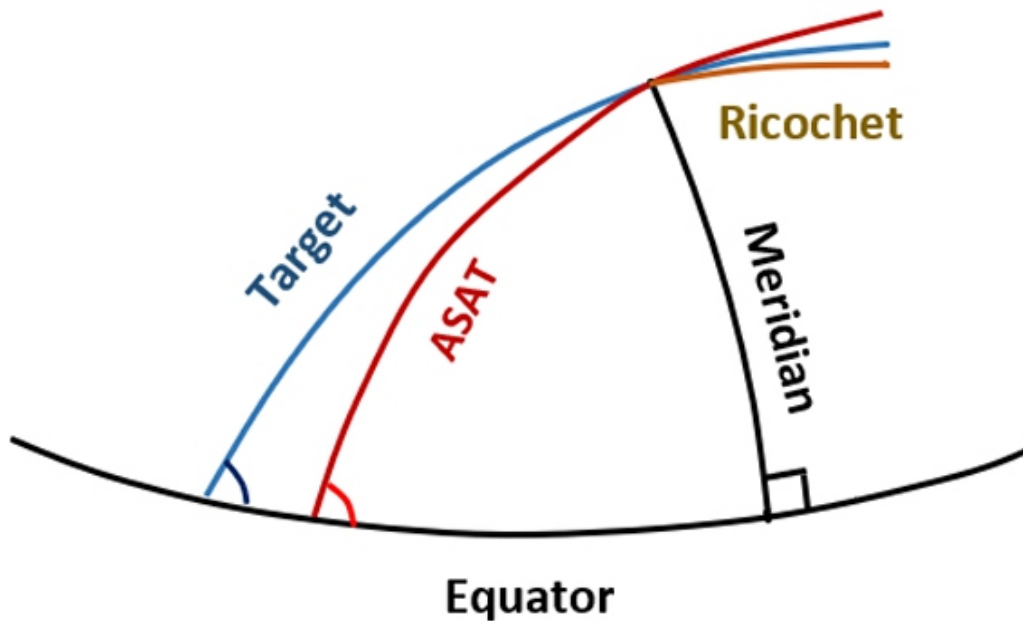


Figure 1

The orbital elements data disclose that the fragments of Cosmos 1408 and the ASAT were in the same energy levels, which suggests that the target velocity and the ASAT velocities were similar prior to the impact. That is how ASAT could hit its target from an angle of 19.9081° . If the ASAT had to hit its target squarely from behind, it would have required far greater speed than the speed of the target in order to be effective.

GABBARD DIAGRAM OF COSMOS 1408 FRAGMENTS

The Gabbard diagram is a simple yet useful tool now-a-days employed in virtually all satellite fragmentation studies. It plots the apogee and perigee heights of the fragmenting satellite and its fragments against their orbital periods. It can shed considerable light on the nature of the fragmentation, the location of the fragmentation point, the directionality and intensity of the fragments' spread, effects of atmospheric drag, etc. Detailed analyses on the formation of the Gabbard diagram and its morphology can be found in Ref. [20].

Figure 2 is the Gabbard diagram plot of the first 510 fragments of Cosmos 1408 (not counting the parent and its largest remnant) cataloged through Day 349 of 2021 (30 days after the event). Out of the 510 fragments, a greater number of fragments (307) fragments had enhanced periods and were located on the right-hand side of the 'inclined X pattern' whereas the rest of the fragments (203) were found on the left-hand side. The latter fragments displayed 'claw-shaped formation' signifying atmospheric drag effects. The true anomaly of the target satellite at breakup point was estimated to be 331o, which is not far from the perigee point where the satellite is at its slowest. The perigee point was also the favorite rendezvous point selected in the Soviet-era ASAT tests. Normally, when a satellite breaks up near its perigee without external perturbative impulses, roughly equal number of fragments are found on either side of the breakup point. The smaller number of fragments on the left (303) suggests that a significant number of fragments receiving negative down-range velocity perturbations had deorbited by the time their orbital elements were ascertained.

A prominent feature of Fig. 2 are the high energy fragments on the far right, now identified as ricochet material from the ASAT. The fractional increase in specific energy of the ricochet dE/E is related to the fractional increase in period dP/P . From the energy equation, one finds:

$$\frac{dE}{E} = -\frac{2}{3} \frac{dP}{P} \quad (2)$$

For the average ricochet in Fig. 2, $P = 112$ min; $P_0 = 94.15$ min; and $dP = 17.85$ min whence: $dE/E = 12.64\%$, a figure quite compatible with those observed in other satellite breakups in orbit [18]. Note that the percentage increase is positive since E is a negative quantity.

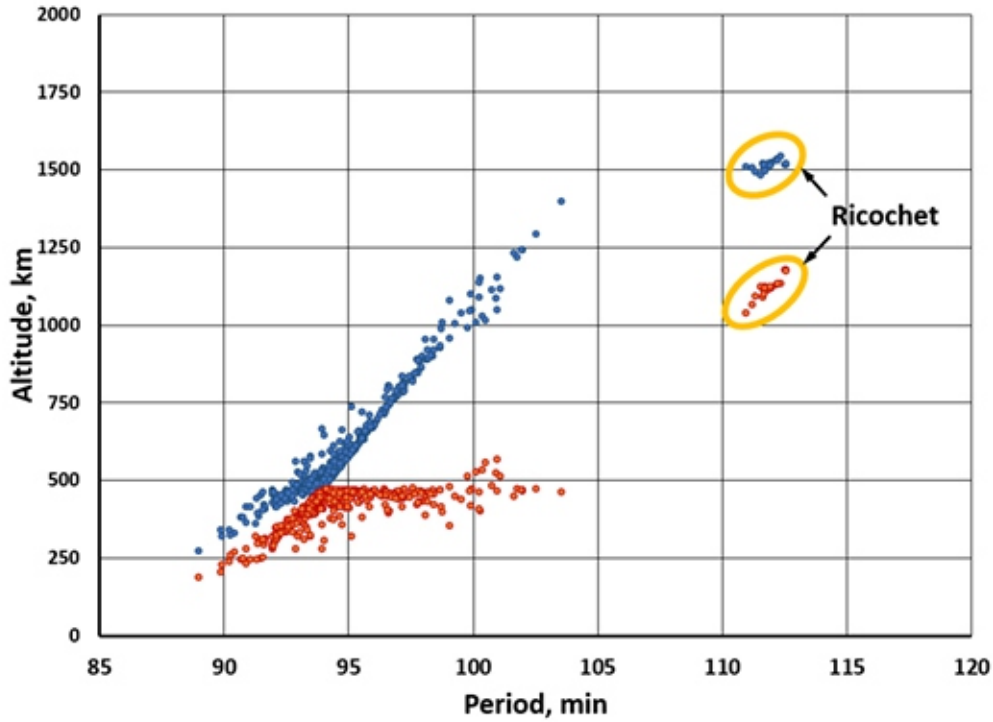


Figure 2

VELOCITY PERTURBATIONS OF COSMOS 1408 FRAGMENTS

The magnitude, variance and directionality of the ejection velocities of the fragments can shed valuable light regarding the nature and intensity of the fragmentation. Badhwar, et al. [19] obtained exact solutions for the velocity perturbations of the fragments of a breakup. In an orthogonal coordinate system with the fragmenting satellite at the origin and the radial \hat{r} , down-range (d) and cross-range (x) directions as the axes, the velocity of the parent satellite at the instance of fragmentation is written

as $\vec{v} = v_r \hat{r} + v_d \hat{d}$, where

$$v_d = \frac{1}{r} \sqrt{\mu a (1 - e^2)} \quad (3)$$

and

$$v_r = \pm \frac{1}{r} \sqrt{\mu a e^2 - \frac{\mu}{a} (r - a)^2} \quad (4)$$

with μ being the **gravitational parameter of the Earth**. In Eq. (4), the + sign corresponds to the **ascending mode** of the satellite whereas the – sign corresponds to the **descending mode**.

Upon fragmentation, the velocity of a fragment has the components $v_r + dv_r$, $v_d + dv_d$ and dv_x , where the **velocity perturbation components of the fragment** are in the three orthogonal directions are given by [19]:

$$dv_r = \pm \sqrt{\mu \left(\frac{2}{r} - \frac{1}{r'} \right) - \frac{\mu a'}{r^2} (1 - e'^2)} - v_r \quad (5)$$

$$dv_d = \frac{\cos \zeta}{r} \sqrt{\mu a' (1 - e'^2)} - v_d \quad (6)$$

and

$$dv_x = \frac{\sin \zeta}{r} \sqrt{\mu a' (1 - e'^2)} \quad (7)$$

In the above equations, the primed quantities pertain to the fragment's orbit, and ζ is the **plane change angle of the fragment's orbit** from the parent's orbit. In Eq. (5), the + sign corresponds to the **ascending mode** of the fragment and the – sign corresponds to the **descending mode**. The plane change angle ζ is calculated from the inclinations of the parent's and fragment's orbits and the **latitude of the breakup point** λ by utilizing Eq. (1).

Table I gives a summary of the velocity perturbations (dv_r , dv_d and dv_x), their ranges, frequencies and counts. Also entered in the table are the **total ejection speeds** $dv = \sqrt{dv_r^2 + dv_d^2 + dv_x^2}$. As indicated earlier, the dv_d s were more numerous in the positive direction (307) than in the negative (203), indicating partially because the ASAT struck its target generally from behind [13, 14], but more likely because atmospheric drag had de-orbited many fragments. As for the dv_x s, more fragments were deflected in the positive cross-range direction (285) than in the negative (225), which is consisted with the fact that the ASAT struck its target slightly from the right when viewed from above the horizontal plane (Fig. 1). In the radial direction, many (139) of the dv_r s calculations were indeterminate. This happens when the orbits of the parent and the fragment no longer intersect and the discriminant in Eq. (5) becomes imaginary. As is customary, the latter is then set equal to zero, whence dv_r assumes the value of $-v_r$. Not counting these values, there were almost equal number of fragments above (182) and below (185) the horizontal plane.

Figure 3 is a scatterplot of the Cosmos 1408 fragments in the local horizontal plane at the breakup point. The fragment scatter on both sides of the cross-range direction were extensive as were the ranges of scatter. The range of scatter in the down-range direction

was smaller, particularly on the back side. The ricochet fragments (marked within the oval) were found in the farthest down-range direction with an average angle of -2.018° to the right of the forward direction. Interestingly, the remnant of the target satellite was deflected $.0368^\circ$ to the left of forward direction, possibly displaying recoil effect with the ricochet fragments.

Figure 4 is the scatterplot of the Cosmos 1408 fragments in a local vertical plane containing the orbital plane of the fragmenting satellite. The fragment scatter shows some resemblance with that of Fig. 3, but with a smaller range in the vertical coordinate.

The ricochet fragments (marked within the oval) were once again located in the farthest down-range direction. The fragments spread displayed a prominent ‘butterfly pattern’ above and below the horizontal plane similar to one first observed in the Spot-1 Ariane rocket fragmentation event [20]. Since it was convincingly argued that the butterfly pattern of the latter event was the result of the impact of a small debris upon the Ariane rocket [20] and since no such pattern was ever observed in any of the explosive fragmentations of rocket bodies in orbit, the occurrence of such a pattern can now be taken as ‘another sufficient condition for collision in space’.

Table I. Velocity perturbations of the Cosmos 1408 Fragments and Fragment Counts

	dv_d , m/s	dv_x , m/s	dv_r , m/s	dv , m/s
Maximum	466.90	703.71	296.84	704.85
Average	31.76	10.06	2.43	150.09
Minimum	-148.37	-661.40	-227.40	7.30
Range	615.27	1,365.11	524.24	697.55
Positive count	307	285	182	510
Negative count	203	225	185	–
Indeterminate	0	0	143	–
Total count	510	510	510	510

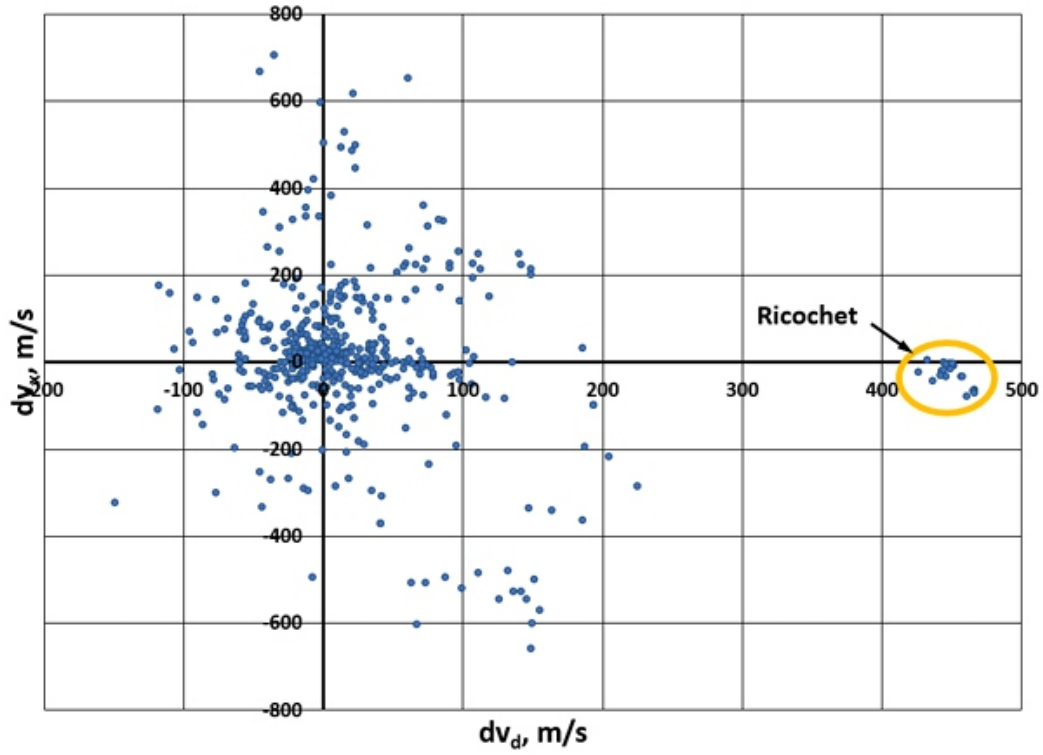


Figure 3

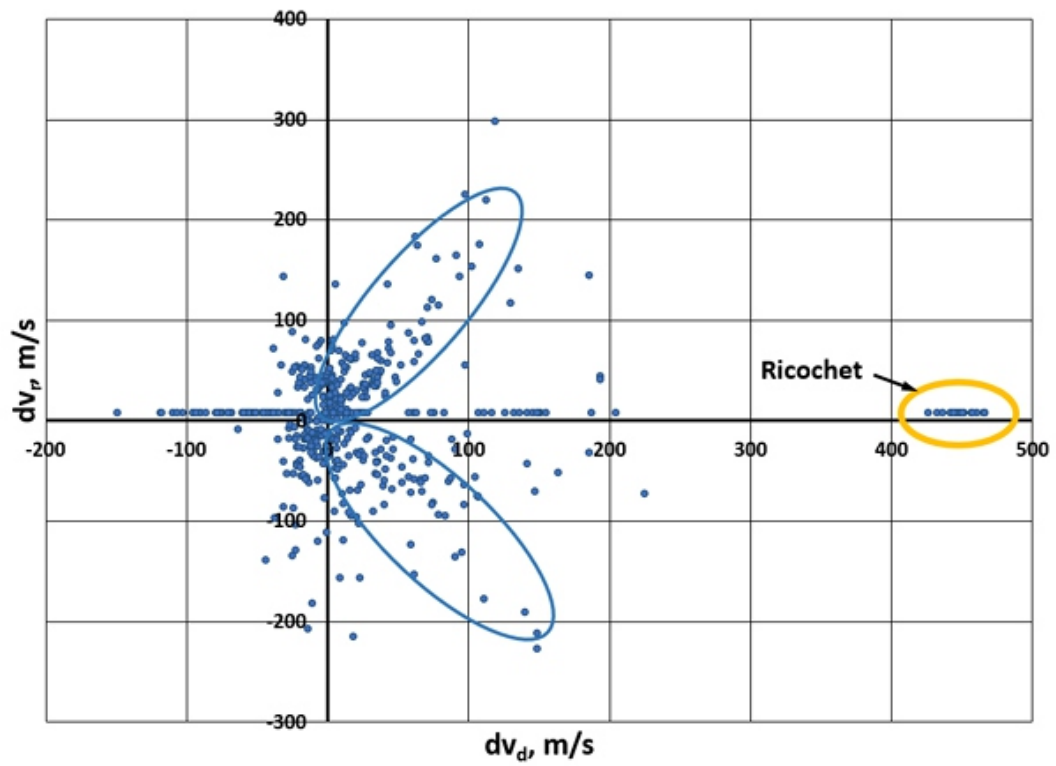


Figure 4

ANGULAR DISTRIBUTION OF COSMOS 1408 FRAGMENTS

In the fragmenting satellite's frame of reference, the direction of the velocity perturbation of a fragment may be defined by two angles akin to the latitude and longitude of the globe. The velocity perturbation components dv_d , dv_x and dv_r form a right-handed orthogonal coordinate system, with dv_d and dv_x defining a local horizontal plane; and dv_r , and dv_d defining the plane of the orbit. The two angular coordinates are: (1) the local latitude λ , measured from the horizontal plane; and (2) the local longitude ϕ , measured from the plane of the orbit [20]:

$$\lambda = \sin^{-1}\left(\frac{dv_r}{dv}\right) \tag{8}$$

and

$$\phi = \tan^{-1}\left(\frac{dv_x}{dv_d}\right) + n\pi \tag{9}$$

where $n = 0$ if $dv_d > 0$; $n = 1$ if $dv_d < 0$ and $dv_x > 0$; and $n = -1$ if $dv_d < 0$ and $dv_x < 0$. λ ranges from $-\pi/2$ to $\pi/2$; whereas ϕ ranges from $-\pi$ to π . The eight octants of threedimensional space are defined in accordance to the scheme indicated in Table II [21]. Figure 5 depicts the dispersion of the Cosmos-1408 fragments on an equidistant cylindrical projection map in the local angular coordinates at the breakup point with the octants of space clearly marked. On the whole, the fragments are more or less randomly placed, albeit with a few concentration areas. The high-energy ricochet fragments are marked near the center of the map, indicating that they headed mainly towards the positive down-range direction. The concentration along the local equator includes most of those fragments whose dv_r s were indeterminate. There is a major concentration area south of the local equator in Octant V, bordering and extending into Octant VI populated by fragments having positive dv_x s and negative dv_r s (vide Table II). These two octants are situated just below Octants I and II respectively (Table II), where $dv_x > 0$; and $dv_r < 0$.

Table II. Octants of Space

Octant	dv_d	dv_x	dv_r	Location	
				Horizontal Plane	Vertical Direction
I	+	+	+	Between IV & II	Above V
II	-	+	+	Between I & III	Above VI
III	-	-	+	Between II & IV	Above VII
IV	+	-	+	Between IV & I	Above VIII
V	+	+	-	Between VIII & VI	Below I
VI	-	+	-	Between V & VII	Below II
VII	-	-	-	Between VI & VIII	Below III
VIII	+	-	-	Between VII & V	Below IV

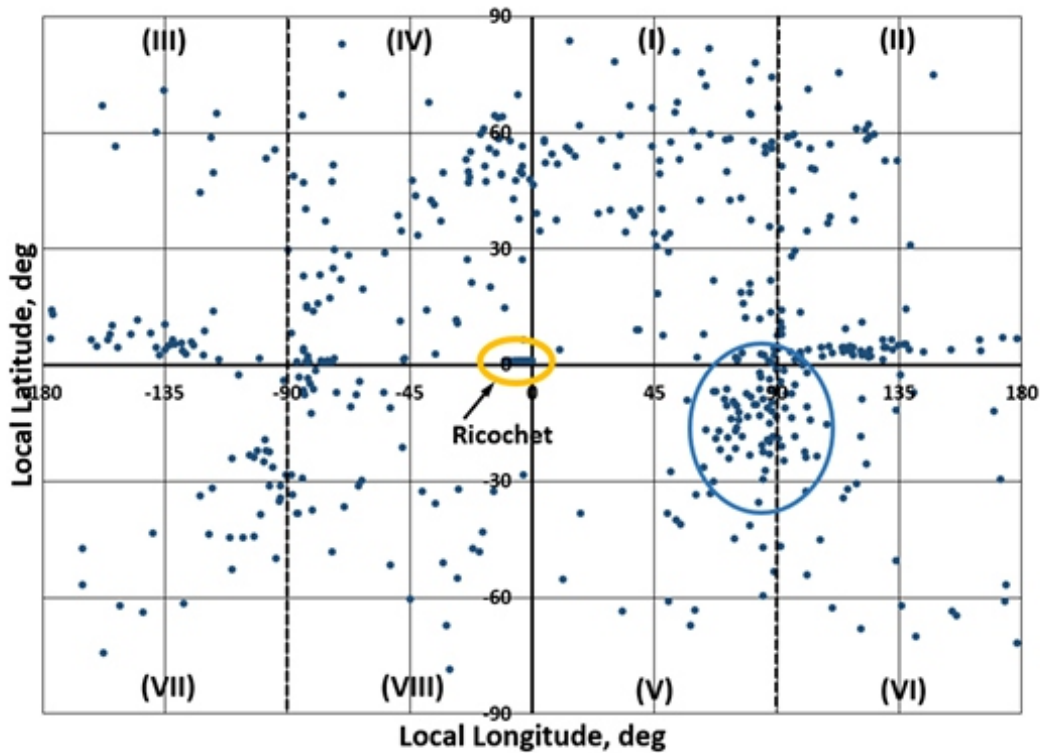


Figure 5

CONCLUSIONS

In this paper, Russia's direct-ascent ASAT test of 15 November 2021 was investigated and the following highlights were uncovered.

1. The Nudol ASAT missile launched from Plesetsk Cosmodrome was different from the earlier direct-ascent ASAT systems of the United States, China and India. Whereas the earlier systems used sub-orbital trajectories, the Russian ASAT actually attained orbital trajectory prior to hitting its target.
2. Unlike the earlier ASAT systems, the Russian ASAT actually produced an ASAT cloud, thus confirming that it had already attained orbital trajectory.
3. Unlike the earlier ASAT tests where the ASATs hit their targets from the side or from a head-on direction, the Russian ASAT generally came from behind and thus retained some feature of the old Soviet co-orbital method.
4. The Russian ASAT test produced high-energy ricochet fragments (first observed in the US ASAT test of 1985) which satisfied the sufficient condition for collision in space.
5. The butterfly pattern displayed in the fragments spread for only the second time in satellite fragmentation history can now be portrayed as yet another sufficient condition for collision in space.

REFERENCES

- [1] N.L. Johnson, *Artificial Satellite Breakup (Part 2): Soviet Anti-Satellite Program*, *J. Brit. Interplanet. Soc.*, 36, 357-362 (1983).
- [2] A.A. Siddiqi, *The Soviet co-orbital Anti-satellite System: A Synopsis*, *J. Brit. Interplanet. Soc.*, 50, 225-240 (1997).
- [3] A. Tan, V. Edwards, & M. Schamschula, *Fragments Analyses of the Soviet Anti-Satellite Tests – Round 1*, *Adv. Aerospace Sci. & Appl.*, 4, 21-33 (2014).
- [4] R. Kling, *Postmortem of a Hypervelocity Impact*, *Teledyne Brown Engineering Report CS86-LKD-001* (1986).
- [5] S.K. Remillard, *Debris Production in Hypervelocity Impact ASAT Experiments*, M.S. Thesis, U.S. Air Force Institute of Technology (1990).
- [6] A. Tan, G.D. Badhwar, F.A. Allahdadi & D.F. Medina, *Analysis of the Solwind Fragmentation Event Using Theory and Computations*, *J. Spacecr. Rockets*, 33, 79-85 (1996).
- [7] *Orbital Debris Quarterly News*, 11(2), 1-2 (2007).
- [8] A. Tan & M. Dokhanian, *Velocity Perturbations Analysis of the Fengyun-1C Satellite Fragmentation Event*, *Adv. Aerospace Sci.*, 3, 35-46 (2013).
- [9] *Orbital Debris Quarterly News*, 23(3), 1-2 (2019).
- [10] A. Tan, R.C. Reynolds & R. Ramachandran, *Posthumous analysis of the Indian Anti-Satellite Experiment: Puzzles and Answers*, *Adv. Aerospace Sci. Appl.*, 10, 1–10 (2020).
- [11] *Orbital Debris Quarterly News*, 26(1), 1–5, March 2022.
- [12] <https://planet4589.org/space/asat/nudol.html>.
- [13] <https://defense.info/williams-foundation/2022/01/pursuing-a-scorched-earth-orbit-policy-asats-and-space-debris/>
- [14] <https://leolabs-space.com/part-ii-new-observations-on-cosmos-1408-breakup3d8e5441f720>.
- [15] <https://www.space-track.org/>
- [16] N.L. Johnson, *The Collision of Satellites 16937 and 16938*, *Teledyne Brown Engg. Rept. CS87-LKD-001* (1986).
- [17] A. Tan & D. Zhang, *Analysis and Interpretation of the Delta-180 Collision Experiment in Space*, *J. Astronaut. Sci.*, 49, 585-599 (2001).
- [18] A. Tan, *Ricochet Fragments: A Sufficient Condition for Collision in Space?*, *Orbital Debris Monitor*, 9(3), 4-7 (1996).
- [19] G.D. Badhwar, A. Tan, & R.C. Reynolds, *J. Spacecr. Rockets*, 27, 299-305 (1990).
- [20] A. Tan & R. Ramachandran, *Velocity perturbations analysis of the Spot-1 Ariane rocket fragmentation*, *J. Astronaut. Sci.*, 53, 39-50 (2005).
- [21] A. Tan & R.C. Reynolds, *Theory of Satellite Fragmentation in Orbit*, *World Scientific* (2020), pp.

Instructions for Authors

Essentials for Publishing in this Journal

- 1 Submitted articles should not have been previously published or be currently under consideration for publication elsewhere.
- 2 Conference papers may only be submitted if the paper has been completely re-written (taken to mean more than 50%) and the author has cleared any necessary permission with the copyright owner if it has been previously copyrighted.
- 3 All our articles are refereed through a double-blind process.
- 4 All authors must declare they have read and agreed to the content of the submitted article and must sign a declaration correspond to the originality of the article.

Submission Process

All articles for this journal must be submitted using our online submissions system. <http://enrichedpub.com/> . Please use the Submit Your Article link in the Author Service area.

Manuscript Guidelines

The instructions to authors about the article preparation for publication in the Manuscripts are submitted online, through the e-Ur (Electronic editing) system, developed by **Enriched Publications Pvt. Ltd.** The article should contain the abstract with keywords, introduction, body, conclusion, references and the summary in English language (without heading and subheading enumeration). The article length should not exceed 16 pages of A4 paper format.

Title

The title should be informative. It is in both Journal's and author's best interest to use terms suitable. For indexing and word search. If there are no such terms in the title, the author is strongly advised to add a subtitle. The title should be given in English as well. The titles precede the abstract and the summary in an appropriate language.

Letterhead Title

The letterhead title is given at a top of each page for easier identification of article copies in an Electronic form in particular. It contains the author's surname and first name initial .article title, journal title and collation (year, volume, and issue, first and last page). The journal and article titles can be given in a shortened form.

Author's Name

Full name(s) of author(s) should be used. It is advisable to give the middle initial. Names are given in their original form.

Contact Details

The postal address or the e-mail address of the author (usually of the first one if there are more Authors) is given in the footnote at the bottom of the first page.

Type of Articles

Classification of articles is a duty of the editorial staff and is of special importance. Referees and the members of the editorial staff, or section editors, can propose a category, but the editor-in-chief has the sole responsibility for their classification. Journal articles are classified as follows:

Scientific articles:

1. Original scientific paper (giving the previously unpublished results of the author's own research based on management methods).
2. Survey paper (giving an original, detailed and critical view of a research problem or an area to which the author has made a contribution visible through his self-citation);
3. Short or preliminary communication (original management paper of full format but of a smaller extent or of a preliminary character);
4. Scientific critique or forum (discussion on a particular scientific topic, based exclusively on management argumentation) and commentaries. Exceptionally, in particular areas, a scientific paper in the Journal can be in a form of a monograph or a critical edition of scientific data (historical, archival, lexicographic, bibliographic, data survey, etc.) which were unknown or hardly accessible for scientific research.

Professional articles:

1. Professional paper (contribution offering experience useful for improvement of professional practice but not necessarily based on scientific methods);
2. Informative contribution (editorial, commentary, etc.);
3. Review (of a book, software, case study, scientific event, etc.)

Language

The article should be in English. The grammar and style of the article should be of good quality. The systematized text should be without abbreviations (except standard ones). All measurements must be in SI units. The sequence of formulae is denoted in Arabic numerals in parentheses on the right-hand side.

Abstract and Summary

An abstract is a concise informative presentation of the article content for fast and accurate Evaluation of its relevance. It is both in the Editorial Office's and the author's best interest for an abstract to contain terms often used for indexing and article search. The abstract describes the purpose of the study and the methods, outlines the findings and state the conclusions. A 100- to 250-Word abstract should be placed between the title and the keywords with the body text to follow. Besides an abstract are advised to have a summary in English, at the end of the article, after the Reference list. The summary should be structured and long up to 1/10 of the article length (it is more extensive than the abstract).

Keywords

Keywords are terms or phrases showing adequately the article content for indexing and search purposes. They should be allocated heaving in mind widely accepted international sources (index, dictionary or thesaurus), such as the Web of Science keyword list for science in general. The higher their usage frequency is the better. Up to 10 keywords immediately follow the abstract and the summary, in respective languages.

Acknowledgements

The name and the number of the project or programmed within which the article was realized is given in a separate note at the bottom of the first page together with the name of the institution which financially supported the project or programmed.

Tables and Illustrations

All the captions should be in the original language as well as in English, together with the texts in illustrations if possible. Tables are typed in the same style as the text and are denoted by numerals at the top. Photographs and drawings, placed appropriately in the text, should be clear, precise and suitable for reproduction. Drawings should be created in Word or Corel.

Citation in the Text

Citation in the text must be uniform. When citing references in the text, use the reference number set in square brackets from the Reference list at the end of the article.

Footnotes

Footnotes are given at the bottom of the page with the text they refer to. They can contain less relevant details, additional explanations or used sources (e.g. scientific material, manuals). They cannot replace the cited literature.

The article should be accompanied with a cover letter with the information about the author(s): surname, middle initial, first name, and citizen personal number, rank, title, e-mail address, and affiliation address, home address including municipality, phone number in the office and at home (or a mobile phone number). The cover letter should state the type of the article and tell which illustrations are original and which are not.

